

First Very Long Baseline Interferometry Detections at 870 μm

ALEXANDER W. RAYMOND,^{1,2,3} SHEPERD S. DOELEMEN,^{1,2,*} KEIICHI ASADA,⁴ LINDY BLACKBURN,^{1,2} GEOFFREY C. BOWER,^{5,6} MICHAEL BREMER,⁷ DOMINIQUE BROGUIERE,⁷ MING-TANG CHEN,⁴ GEOFFREY B. CREW,⁸ SVEN DORNBUSCH,⁹ VINCENT L. FISH,⁸ ROBERTO GARCÍA,⁷ OLIVIER GENTAZ,⁷ CIRIACO GODDI,^{10,11} CHIH-CHIANG HAN,⁴ MICHAEL H. HECHT,⁸ YAU-DE HUANG,⁴ MICHAEL JANSSEN,^{12,9} GARRETT K. KEATING,² JUN YI KOAY,⁴ THOMAS P. KRICHBAUM,⁹ WEN-PING LO,^{4,13} SATOKI MATSUSHITA,⁴ LYNN D. MATTHEWS,⁸ JAMES M. MORAN,^{1,2} TIMOTHY J. NORTON,² NIMESH PATEL,² DOMINIC W. PESCE,^{2,1} VENKATESH RAMAKRISHNAN,^{14,15,16} HELGE ROTTMANN,⁹ ALAN L. ROY,⁹ SALVADOR SÁNCHEZ,¹⁷ REMO P. J. TILANUS,¹⁸ MICHAEL TITUS,⁸ PABLO TORNE,^{17,9} JAN WAGNER,⁹ JONATHAN WEINTROUB,^{1,2} MACIEK WIELGUS,⁹ ANDRÉ YOUNG,¹² KAZUNORI AKIYAMA,^{8,19,1} EZEQUIEL ALBENTOSA-RUÍZ,²⁰ ANTXON ALBERDI,²¹ WALTER ALEF,⁹ JUAN CARLOS ALGABA,²² RICHARD ANANTUA,^{1,2,23} REBECCA AZULAY,^{20,24,9} UWE BACH,⁹ ANNE-KATHRIN BACZKO,^{25,9} DAVID BALL,¹⁸ MISLAV BALOKOVIĆ,²⁶ BIDISHA BANDYOPADHYAY,²⁷ JOHN BARRETT,⁸ MICH BAUBÖCK,²⁸ BRADFORD A. BENSON,^{29,30} DAN BINTLEY,^{31,32} RAYMOND BLUNDELL,² KATHERINE L. BOUMAN,³³ HOPE BOYCE,^{34,35} ROGER BRISSENDEN,^{1,2} SILKE BRITZEN,⁹ AVERY E. BRODERICK,^{36,37,38} THOMAS BRONZWAER,¹² SANDRA BUSTAMANTE,³⁹ JOHN E. CARLSTROM,^{40,30,41,42} ANDREW CHAEL,⁴³ CHI-KWAN CHAN,^{18,44,45} DOMINIC O. CHANG,^{1,2} KOUSHIK CHATTERJEE,^{1,2} SHAMI CHATTERJEE,⁴⁶ YONGJUN CHEN (陈永军),^{47,48} XIAOPENG CHENG,⁴⁹ ILJE CHO,^{21,49,50} PIERRE CHRISTIAN,⁵¹ NICHOLAS S. CONROY,^{52,2} JOHN E. CONWAY,²⁵ THOMAS M. CRAWFORD,^{30,40} ALEJANDRO CRUZ-OSORIO,^{53,54} YUZHU CUI (崔玉竹),^{55,56} ROHAN DAHALE,²¹ JORDY DAVELAAR,^{57,58,12} MARIAFELICIA DE LAURENTIS,^{59,60} ROGER DEANE,^{61,62,63} JESSICA DEMPSEY,^{31,32,64} GREGORY DESVIGNES,^{9,65} JASON DEXTER,⁶⁶ VEDANT DHRUV,²⁸ INDU K. DIHINGIA,⁵⁶ SERGIO A. DZIB,^{67,9} RALPH P. EATOUGH,^{68,9} RAZIEH EMAMI,² HEINO FALCKE,¹² JOSEPH FARAH,^{69,70} EDWARD FOMALONT,⁷¹ ANNE-LAURE FONTANA,⁶⁷ H. ALYSON FORD,¹⁸ MARIANNA FOSCHI,²¹ RAQUEL FRAGA-ENCINAS,¹² WILLIAM T. FREEMAN,^{72,73} PER FRIBERG,^{31,32} CHRISTIAN M. FROMM,^{74,54,9} ANTONIO FUENTES,²¹ PETER GALISON,^{1,75,76} CHARLES F. GAMMIE,^{28,52,77} BORIS GEORGIEV,¹⁸ ROMAN GOLD,⁷⁸ ARTURO I. GÓMEZ-RUIZ,^{79,80} JOSÉ L. GÓMEZ,²¹ MINFENG GU (顾敏峰),^{47,81} MARK GURWELL,² KAZUHIRO HADA,^{82,83} DARYL HAGGARD,^{34,35} RONALD HESPER,⁸⁴ DIRK HEUMANN,¹⁸ LUIS C. HO (何子山),^{85,86} PAUL HO,^{4,32,31} MAREKI HONMA,^{82,83,87} CHIH-WEI L. HUANG,⁴ LEI HUANG (黄磊),^{47,81} DAVID H. HUGHES,⁷⁹ SHIRO IKEDA,^{19,88,89,90} C. M. VIOLETTE IMPELLIZZERI,^{91,71} MAKOTO INOUE,⁴ SARA ISSAOUN,^{2,92} DAVID J. JAMES,^{93,94} BUELL T. JANNUZI,¹⁸ BRITTON JETER,⁴ WU JIANG (江悟),⁴⁷ ALEJANDRA JIMÉNEZ-ROSALES,¹² MICHAEL D. JOHNSON,^{1,2} SVETLANA JORSTAD,⁹⁵ ADAM C. JONES,³⁰ ABHISHEK V. JOSHI,²⁸ TAEHYUN JUNG,^{49,96} RAMESH KARUPPUSAMY,⁹ TOMOHISA KAWASHIMA,⁹⁷ MARK KETTENIS,⁹⁸ DONG-JIN KIM,⁸ JAE-YOUNG KIM,^{99,9} JONGSOO KIM,⁴⁹ JUNHAN KIM,¹⁰⁰ MOTOKI KINO,^{19,101} PRASHANT KOCHERLAKOTA,⁵⁴ YUTARO KOFUJI,^{82,87} PATRICK M. KOCH,⁴ SHOKO KOYAMA,^{102,4} CARSTEN KRAMER,⁶⁷ JOANA A. KRAMER,⁹ MICHAEL KRAMER,⁹ DEREK KUBO,⁵ CHENG-YU KUO,^{103,4} NOEMI LA BELLA,¹² SANG-SUNG LEE,⁴⁹ AVIAD LEVIS,³³ ZHIYUAN LI (李志远),^{104,105} ROCCO LICO,^{106,21} GREG LINDAHL,² MICHAEL LINDQVIST,²⁵ MIKHAIL LISAKOV,⁹ JUN LIU (刘俊),⁹ KUO LIU,⁹ ELISABETTA LIUZZO,¹⁰⁷ ANDREI P. LOBANOV,⁹ LAURENT LOINARD,¹⁰⁸ COLIN J. LONSDALE,⁸ AMY E. LOWITZ,¹⁸ RU-SEN LU (路如森),^{47,48,9} NICHOLAS R. MACDONALD,⁹ SYLVAIN MAHIEU,⁶⁷ DORIS MAIER,⁶⁷ JIRONG MAO (毛基荣),^{109,110,111} NICOLA MARCHILI,^{107,9} SERA MARKOFF,^{112,113} DANIEL P. MARRONE,¹⁸ ALAN P. MARSCHER,⁹⁵ IVÁN MARTÍ-VIDAL,^{20,24} LIA MEDEIROS,^{114,92} KARL M. MENTEN,⁹ IZUMI MIZUNO,^{31,32} YOSUKE MIZUNO,^{56,115,54} JOSHUA MONTGOMERY,^{35,30} KOTARO MORIYAMA,^{54,82} MONIKA MOSCIBRODZKA,¹² WANGA MULAUDZI,¹¹² CORNELIA MÜLLER,^{9,12} HENDRIK MÜLLER,⁹ ALEJANDRO MUS,^{20,24} GIBWA MUSOKE,^{112,12} IOANNIS MYSERLIS,¹¹⁶ HIROSHI NAGAI,^{19,83} NEIL M. NAGAR,²⁷ MASANORI NAKAMURA,^{117,4} GOPAL NARAYANAN,³⁹ INIYAN NATARAJAN,^{2,1} ANTONIOS NATHANAIL,^{118,54} SANTIAGO NAVARRO FUENTES,¹¹⁶ JOEY NEILSEN,¹¹⁹ CHUNCHONG NI,^{37,38,36} MICHAEL A. NOWAK,¹²⁰ JUNGHWAN OH,⁹⁸ HIROKI OKINO,^{82,87} HÉCTOR RAÚL OLIVARES SÁNCHEZ,¹²¹ TOMOAKI OYAMA,⁸² FERYAL ÖZEL,¹²² DANIEL C. M. PALUMBO,^{1,2} GEORGIOS FILIPPOS PARASCHOS,⁹ JONGHO PARK,¹²³ HARRIET PARSONS,^{31,32} UE-LI PEN,^{4,36,124,125,126} VINCENT PIÉTU,⁶⁷ ALEKSANDAR POPSTEFANIJA,³⁹ OLIVER PORTH,^{112,54} BEN PRATHER,²⁸ GIACOMO PRINCIPE,^{127,128,106} DIMITRIOS PSALTIS,¹²² HUNG-YI PU,^{129,130,4} PHILIPPE A. RAFFIN,⁴ RAMPRASAD RAO,² MARK G. RAWLINGS,^{131,31,32} ANGELO RICARTE,^{1,2} BART RIPPERDA,^{124,132,125,36} FREEK ROELOFS,^{2,1,12} CRISTINA ROMERO-CAÑIZALES,⁴ EDUARDO ROS,⁹ ARASH ROSHANINESHAT,¹⁸ IGNACIO RUIZ,¹¹⁶ CHET RUSZCZYK,⁸ KAZI L. J. RYGL,¹⁰⁷ DAVID SÁNCHEZ-ARGÜELLES,^{79,80} MIGUEL SÁNCHEZ-PORTAL,¹¹⁶ MAHITO SASADA,^{133,82,134} KAUSHIK SATAPATHY,¹⁸ TUOMAS SAVOLAINEN,^{135,136,9} F. PETER SCHLOERB,³⁹ JONATHAN SCHONFELD,² KARL-FRIEDRICH SCHUSTER,⁶⁷ LIJING SHAO,^{86,9} ZHIQIANG SHEN (沈志强),^{47,48} DES SMALL,⁹⁸ BONG WON SOHN,^{49,96,50} JASON SOOHOO,⁸ LEÓN DAVID SOSAPANTA SALAS,¹¹² KAMAL SOUCCAR,³⁹ RANJANI SRINIVASAN,² JOSHUA S. STANWAY,¹³⁷ HE SUN (孙赫),^{138,139} FUMIE TAZAKI,¹⁴⁰ ALEXANDRA J. TETARENKO,¹⁴¹ PAUL TIEDE,^{2,1} KENJI TOMA,^{142,143} TERESA TOSCANO,²¹ EFTHALIA TRAIANOÛ,^{21,9} TYLER TRENT,¹⁸ SASCHA TRIPPE,¹⁴⁴ MATTHEW TURK,⁵² ILSE VAN BEMMEL,⁹⁸ HUIB JAN VAN LANGEVELDE,^{98,91,145} DANIEL R. VAN ROSSUM,¹² JESSE VOS,¹² DEREK WARD-THOMPSON,¹³⁷ JOHN WARDLE,¹⁴⁶ JASMIN E. WASHINGTON,¹⁸ ROBERT WHARTON,⁹ KAJ WIJK,¹⁴⁷ GUNTHER WITZEL,⁹ MICHAEL F. WONDRAK,^{12,148} GEORGE N. WONG,^{149,43} QINGWEN WU (吴庆文),¹⁵⁰ NITIKA YADLAPALLI,³³ PAUL YAMAGUCHI,² ARISTOMENIS YFANTIS,¹² DOOSOO YOON,¹¹² ZIRI YOUNSI,^{151,54} WEI YU (于威),² FENG YUAN (袁峰),¹⁵² YE-FEI YUAN (袁业飞),¹⁵³ J. ANTON ZENSUS,⁹ SHUO ZHANG,¹⁵⁴ GUANG-YAO ZHAO,^{21,9} AND SHAN-SHAN ZHAO (赵杉杉)⁴⁷

¹Black Hole Initiative at Harvard University, 20 Garden Street, Cambridge, MA 02138, USA

²Center for Astrophysics | Harvard & Smithsonian, 60 Garden Street, Cambridge, MA 02138, USA

³Current address is Jet Propulsion Laboratory, California Institute of Technology, Pasadena, CA, USA

- ⁴*Institute of Astronomy and Astrophysics, Academia Sinica, 11F of Astronomy-Mathematics Building, AS/NTU No. 1, Sec. 4, Roosevelt Rd., Taipei 106216, Taiwan, R.O.C.*
- ⁵*Institute of Astronomy and Astrophysics, Academia Sinica, 645 N. A'ohoku Place, Hilo, HI 96720, USA*
- ⁶*Department of Physics and Astronomy, University of Hawaii at Manoa, 2505 Correa Road, Honolulu, HI 96822, USA*
- ⁷*Institut de Radioastronomie Millimétrique, 300 rue de la Piscine, F-38406 Saint Martin d'Hères, France*
- ⁸*Massachusetts Institute of Technology Haystack Observatory, 99 Millstone Road, Westford, MA 01886, USA*
- ⁹*Max-Planck-Institut für Radioastronomie, Auf dem Hügel 69, D-53121 Bonn, Germany*
- ¹⁰*Dipartimento di Fisica, Università degli Studi di Cagliari, SP Monserrato-Sestu km 0.7, I-09042 Monserrato, Italy*
- ¹¹*INAF - Osservatorio Astronomico di Cagliari, Via della Scienza 5, 09047, Selargius, CA, Italy*
- ¹²*Department of Astrophysics, Institute for Mathematics, Astrophysics and Particle Physics (IMAPP), Radboud University, P.O. Box 9010, 6500 GL Nijmegen, The Netherlands*
- ¹³*Department of Physics, National Taiwan University, No.1, Sect.4, Roosevelt Rd., Taipei 106216, Taiwan, R.O.C*
- ¹⁴*Astronomy Department, Universidad de Concepción, Casilla 160-C, Concepción, Chile*
- ¹⁵*Finnish Centre for Astronomy with ESO, FI-20014 University of Turku, Finland*
- ¹⁶*Aalto University Metsähovi Radio Observatory, Metsähovintie 114, FI-02540 Kylmälahti, Finland*
- ¹⁷*Institut de Radioastronomie Millimétrique, Avenida Divina Pastora 7, Local 20, E-18012, Granada, Spain*
- ¹⁸*Steward Observatory and Department of Astronomy, University of Arizona, 933 N. Cherry Ave., Tucson, AZ 85721, USA*
- ¹⁹*National Astronomical Observatory of Japan, 2-21-1 Osawa, Mitaka, Tokyo 181-8588, Japan*
- ²⁰*Departament d'Astronomia i Astrofísica, Universitat de València, C. Dr. Moliner 50, E-46100 Burjassot, València, Spain*
- ²¹*Instituto de Astrofísica de Andalucía-CSIC, Glorieta de la Astronomía s/n, E-18008 Granada, Spain*
- ²²*Department of Physics, Faculty of Science, Universiti Malaya, 50603 Kuala Lumpur, Malaysia*
- ²³*Department of Physics & Astronomy, The University of Texas at San Antonio, One UTSA Circle, San Antonio, TX 78249, USA*
- ²⁴*Observatori Astronòmic, Universitat de València, C. Catedrático José Beltrán 2, E-46980 Paterna, València, Spain*
- ²⁵*Department of Space, Earth and Environment, Chalmers University of Technology, Onsala Space Observatory, SE-43992 Onsala, Sweden*
- ²⁶*Yale Center for Astronomy & Astrophysics, Yale University, 52 Hillhouse Avenue, New Haven, CT 06511, USA*
- ²⁷*Astronomy Department, Universidad de Concepción, Casilla 160-C, Concepción, Chile*
- ²⁸*Department of Physics, University of Illinois, 1110 West Green Street, Urbana, IL 61801, USA*
- ²⁹*Fermi National Accelerator Laboratory, MS209, P.O. Box 500, Batavia, IL 60510, USA*
- ³⁰*Department of Astronomy and Astrophysics, University of Chicago, 5640 South Ellis Avenue, Chicago, IL 60637, USA*
- ³¹*East Asian Observatory, 660 N. A'ohoku Place, Hilo, HI 96720, USA*
- ³²*James Clerk Maxwell Telescope (JCMT), 660 N. A'ohoku Place, Hilo, HI 96720, USA*
- ³³*California Institute of Technology, 1200 East California Boulevard, Pasadena, CA 91125, USA*
- ³⁴*Department of Physics, McGill University, 3600 rue University, Montréal, QC H3A 2T8, Canada*
- ³⁵*Trottier Space Institute at McGill, 3550 rue University, Montréal, QC H3A 2A7, Canada*
- ³⁶*Perimeter Institute for Theoretical Physics, 31 Caroline Street North, Waterloo, ON N2L 2Y5, Canada*
- ³⁷*Department of Physics and Astronomy, University of Waterloo, 200 University Avenue West, Waterloo, ON N2L 3G1, Canada*
- ³⁸*Waterloo Centre for Astrophysics, University of Waterloo, Waterloo, ON N2L 3G1, Canada*
- ³⁹*Department of Astronomy, University of Massachusetts, Amherst, MA 01003, USA*
- ⁴⁰*Kavli Institute for Cosmological Physics, University of Chicago, 5640 South Ellis Avenue, Chicago, IL 60637, USA*
- ⁴¹*Department of Physics, University of Chicago, 5720 South Ellis Avenue, Chicago, IL 60637, USA*
- ⁴²*Enrico Fermi Institute, University of Chicago, 5640 South Ellis Avenue, Chicago, IL 60637, USA*
- ⁴³*Princeton Gravity Initiative, Jadwin Hall, Princeton University, Princeton, NJ 08544, USA*
- ⁴⁴*Data Science Institute, University of Arizona, 1230 N. Cherry Ave., Tucson, AZ 85721, USA*
- ⁴⁵*Program in Applied Mathematics, University of Arizona, 617 N. Santa Rita, Tucson, AZ 85721, USA*
- ⁴⁶*Cornell Center for Astrophysics and Planetary Science, Cornell University, Ithaca, NY 14853, USA*
- ⁴⁷*Shanghai Astronomical Observatory, Chinese Academy of Sciences, 80 Nandan Road, Shanghai 200030, People's Republic of China*
- ⁴⁸*Key Laboratory of Radio Astronomy and Technology, Chinese Academy of Sciences, A20 Datun Road, Chaoyang District, Beijing, 100101, People's Republic of China*
- ⁴⁹*Korea Astronomy and Space Science Institute, Daedeok-daero 776, Yuseong-gu, Daejeon 34055, Republic of Korea*
- ⁵⁰*Department of Astronomy, Yonsei University, Yonsei-ro 50, Seodaemun-gu, 03722 Seoul, Republic of Korea*
- ⁵¹*Physics Department, Fairfield University, 1073 North Benson Road, Fairfield, CT 06824, USA*
- ⁵²*Department of Astronomy, University of Illinois at Urbana-Champaign, 1002 West Green Street, Urbana, IL 61801, USA*
- ⁵³*Instituto de Astronomía, Universidad Nacional Autónoma de México (UNAM), Apdo Postal 70-264, Ciudad de México, México*
- ⁵⁴*Institut für Theoretische Physik, Goethe-Universität Frankfurt, Max-von-Laue-Straße 1, D-60438 Frankfurt am Main, Germany*
- ⁵⁵*Research Center for Astronomical Computing, Zhejiang Laboratory, Hangzhou 311100, People's Republic of China*
- ⁵⁶*Tsung-Dao Lee Institute, Shanghai Jiao Tong University, Shengrong Road 520, Shanghai, 201210, People's Republic of China*
- ⁵⁷*Department of Astronomy and Columbia Astrophysics Laboratory, Columbia University, 500 W. 120th Street, New York, NY 10027, USA*

- ⁵⁸*Center for Computational Astrophysics, Flatiron Institute, 162 Fifth Avenue, New York, NY 10010, USA*
- ⁵⁹*Dipartimento di Fisica “E. Pancini”, Università di Napoli “Federico II”, Compl. Univ. di Monte S. Angelo, Edificio G, Via Cinthia, I-80126, Napoli, Italy*
- ⁶⁰*INFN Sez. di Napoli, Compl. Univ. di Monte S. Angelo, Edificio G, Via Cinthia, I-80126, Napoli, Italy*
- ⁶¹*Wits Centre for Astrophysics, University of the Witwatersrand, 1 Jan Smuts Avenue, Braamfontein, Johannesburg 2050, South Africa*
- ⁶²*Department of Physics, University of Pretoria, Hatfield, Pretoria 0028, South Africa*
- ⁶³*Centre for Radio Astronomy Techniques and Technologies, Department of Physics and Electronics, Rhodes University, Makhanda 6140, South Africa*
- ⁶⁴*ASTRON, Oude Hoogeveensedijk 4, 7991 PD Dwingeloo, The Netherlands*
- ⁶⁵*LESIA, Observatoire de Paris, Université PSL, CNRS, Sorbonne Université, Université de Paris, 5 place Jules Janssen, F-92195 Meudon, France*
- ⁶⁶*JILA and Department of Astrophysical and Planetary Sciences, University of Colorado, Boulder, CO 80309, USA*
- ⁶⁷*Institut de Radioastronomie Millimétrique (IRAM), 300 rue de la Piscine, F-38406 Saint Martin d’Hères, France*
- ⁶⁸*National Astronomical Observatories, Chinese Academy of Sciences, 20A Datun Road, Chaoyang District, Beijing 100101, PR China*
- ⁶⁹*Las Cumbres Observatory, 6740 Cortona Drive, Suite 102, Goleta, CA 93117-5575, USA*
- ⁷⁰*Department of Physics, University of California, Santa Barbara, CA 93106-9530, USA*
- ⁷¹*National Radio Astronomy Observatory, 520 Edgemont Road, Charlottesville, VA 22903, USA*
- ⁷²*Department of Electrical Engineering and Computer Science, Massachusetts Institute of Technology, 32-D476, 77 Massachusetts Ave., Cambridge, MA 02142, USA*
- ⁷³*Google Research, 355 Main St., Cambridge, MA 02142, USA*
- ⁷⁴*Institut für Theoretische Physik und Astrophysik, Universität Würzburg, Emil-Fischer-Str. 31, D-97074 Würzburg, Germany*
- ⁷⁵*Department of History of Science, Harvard University, Cambridge, MA 02138, USA*
- ⁷⁶*Department of Physics, Harvard University, Cambridge, MA 02138, USA*
- ⁷⁷*NCSA, University of Illinois, 1205 W. Clark St., Urbana, IL 61801, USA*
- ⁷⁸*CP3-Origins, University of Southern Denmark, Campusvej 55, DK-5230 Odense M, Denmark*
- ⁷⁹*Instituto Nacional de Astrofísica, Óptica y Electrónica. Apartado Postal 51 y 216, 72000. Puebla Pue., México*
- ⁸⁰*Consejo Nacional de Humanidades, Ciencia y Tecnología, Av. Insurgentes Sur 1582, 03940, Ciudad de México, México*
- ⁸¹*Key Laboratory for Research in Galaxies and Cosmology, Chinese Academy of Sciences, Shanghai 200030, People’s Republic of China*
- ⁸²*Mizusawa VLBI Observatory, National Astronomical Observatory of Japan, 2-12 Hoshigaoka, Mizusawa, Oshu, Iwate 023-0861, Japan*
- ⁸³*Department of Astronomical Science, The Graduate University for Advanced Studies (SOKENDAI), 2-21-1 Osawa, Mitaka, Tokyo 181-8588, Japan*
- ⁸⁴*NOVA Sub-mm Instrumentation Group, Kapteyn Astronomical Institute, University of Groningen, Landleven 12, 9747 AD Groningen, The Netherlands*
- ⁸⁵*Department of Astronomy, School of Physics, Peking University, Beijing 100871, People’s Republic of China*
- ⁸⁶*Kavli Institute for Astronomy and Astrophysics, Peking University, Beijing 100871, People’s Republic of China*
- ⁸⁷*Department of Astronomy, Graduate School of Science, The University of Tokyo, 7-3-1 Hongo, Bunkyo-ku, Tokyo 113-0033, Japan*
- ⁸⁸*The Institute of Statistical Mathematics, 10-3 Midori-cho, Tachikawa, Tokyo, 190-8562, Japan*
- ⁸⁹*Department of Statistical Science, The Graduate University for Advanced Studies (SOKENDAI), 10-3 Midori-cho, Tachikawa, Tokyo 190-8562, Japan*
- ⁹⁰*Kavli Institute for the Physics and Mathematics of the Universe, The University of Tokyo, 5-1-5 Kashiwanoha, Kashiwa, 277-8583, Japan*
- ⁹¹*Leiden Observatory, Leiden University, Postbus 2300, 9513 RA Leiden, The Netherlands*
- ⁹²*NASA Hubble Fellowship Program, Einstein Fellow*
- ⁹³*ASTRAVEO LLC, PO Box 1668, Gloucester, MA 01931*
- ⁹⁴*Applied Materials Inc., 35 Dory Road, Gloucester, MA 01930*
- ⁹⁵*Institute for Astrophysical Research, Boston University, 725 Commonwealth Ave., Boston, MA 02215, USA*
- ⁹⁶*University of Science and Technology, Gajeong-ro 217, Yuseong-gu, Daejeon 34113, Republic of Korea*
- ⁹⁷*Institute for Cosmic Ray Research, The University of Tokyo, 5-1-5 Kashiwanoha, Kashiwa, Chiba 277-8582, Japan*
- ⁹⁸*Joint Institute for VLBI ERIC (JIVE), Oude Hoogeveensedijk 4, 7991 PD Dwingeloo, The Netherlands*
- ⁹⁹*Department of Astronomy and Atmospheric Sciences, Kyungpook National University, Daegu 702-701, Republic of Korea*
- ¹⁰⁰*Department of Physics, Korea Advanced Institute of Science and Technology (KAIST), 291 Daehak-ro, Yuseong-gu, Daejeon 34141, Republic of Korea*
- ¹⁰¹*Kogakuin University of Technology & Engineering, Academic Support Center, 2665-1 Nakano, Hachioji, Tokyo 192-0015, Japan*
- ¹⁰²*Graduate School of Science and Technology, Niigata University, 8050 Ikarashi 2-no-cho, Nishi-ku, Niigata 950-2181, Japan*
- ¹⁰³*Physics Department, National Sun Yat-Sen University, No. 70, Lien-Hai Road, Kaosiung City 80424, Taiwan, R.O.C.*
- ¹⁰⁴*School of Astronomy and Space Science, Nanjing University, Nanjing 210023, People’s Republic of China*
- ¹⁰⁵*Key Laboratory of Modern Astronomy and Astrophysics, Nanjing University, Nanjing 210023, People’s Republic of China*
- ¹⁰⁶*INAF-Istituto di Radioastronomia, Via P. Gobetti 101, I-40129 Bologna, Italy*
- ¹⁰⁷*INAF-Istituto di Radioastronomia & Italian ALMA Regional Centre, Via P. Gobetti 101, I-40129 Bologna, Italy*
- ¹⁰⁸*Instituto de Radioastronomía y Astrofísica, Universidad Nacional Autónoma de México, Morelia 58089, México*
- ¹⁰⁹*Yunnan Observatories, Chinese Academy of Sciences, 650011 Kunming, Yunnan Province, People’s Republic of China*
- ¹¹⁰*Center for Astronomical Mega-Science, Chinese Academy of Sciences, 20A Datun Road, Chaoyang District, Beijing, 100012, People’s Republic of China*
- ¹¹¹*Key Laboratory for the Structure and Evolution of Celestial Objects, Chinese Academy of Sciences, 650011 Kunming, People’s Republic of China*
- ¹¹²*Anton Pannekoek Institute for Astronomy, University of Amsterdam, Science Park 904, 1098 XH, Amsterdam, The Netherlands*
- ¹¹³*Gravitation and Astroparticle Physics Amsterdam (GRAPPA) Institute, University of Amsterdam, Science Park 904, 1098 XH Amsterdam, The Netherlands*

- ¹¹⁴*Department of Astrophysical Sciences, Peyton Hall, Princeton University, Princeton, NJ 08544, USA*
- ¹¹⁵*School of Physics and Astronomy, Shanghai Jiao Tong University, 800 Dongchuan Road, Shanghai, 200240, People's Republic of China*
- ¹¹⁶*Institut de Radioastronomie Millimétrique (IRAM), Avenida Divina Pastora 7, Local 20, E-18012, Granada, Spain*
- ¹¹⁷*National Institute of Technology, Hachinohe College, 16-1 Uwanotai, Tamonoki, Hachinohe City, Aomori 039-1192, Japan*
- ¹¹⁸*Research Center for Astronomy, Academy of Athens, Soranou Efessiou 4, 115 27 Athens, Greece*
- ¹¹⁹*Department of Physics, Villanova University, 800 Lancaster Avenue, Villanova, PA 19085, USA*
- ¹²⁰*Physics Department, Washington University, CB 1105, St. Louis, MO 63130, USA*
- ¹²¹*Departamento de Matemática da Universidade de Aveiro and Centre for Research and Development in Mathematics and Applications (CIDMA), Campus de Santiago, 3810-193 Aveiro, Portugal*
- ¹²²*School of Physics, Georgia Institute of Technology, 837 State St NW, Atlanta, GA 30332, USA*
- ¹²³*School of Space Research, Kyung Hee University, 1732, Deogyong-daero, Giheung-gu, Yongin-si, Gyeonggi-do 17104, Republic of Korea*
- ¹²⁴*Canadian Institute for Theoretical Astrophysics, University of Toronto, 60 St. George Street, Toronto, ON M5S 3H8, Canada*
- ¹²⁵*Dunlap Institute for Astronomy and Astrophysics, University of Toronto, 50 St. George Street, Toronto, ON M5S 3H4, Canada*
- ¹²⁶*Canadian Institute for Advanced Research, 180 Dundas St West, Toronto, ON M5G 1Z8, Canada*
- ¹²⁷*Dipartimento di Fisica, Università di Trieste, I-34127 Trieste, Italy*
- ¹²⁸*INFN Sez. di Trieste, I-34127 Trieste, Italy*
- ¹²⁹*Department of Physics, National Taiwan Normal University, No. 88, Sec. 4, Tingzhou Rd., Taipei 116, Taiwan, R.O.C.*
- ¹³⁰*Center of Astronomy and Gravitation, National Taiwan Normal University, No. 88, Sec. 4, Tingzhou Road, Taipei 116, Taiwan, R.O.C.*
- ¹³¹*Gemini Observatory/NSF's NOIRLab, 670 N. A'ohōkū Place, Hilo, HI 96720, USA*
- ¹³²*Department of Physics, University of Toronto, 60 St. George Street, Toronto, ON M5S 1A7, Canada*
- ¹³³*Department of Physics, Tokyo Institute of Technology, 2-12-1 Ookayama, Meguro-ku, Tokyo 152-8551, Japan*
- ¹³⁴*Hiroshima Astrophysical Science Center, Hiroshima University, 1-3-1 Kagamiyama, Higashi-Hiroshima, Hiroshima 739-8526, Japan*
- ¹³⁵*Aalto University Department of Electronics and Nanoengineering, PL 15500, FI-00076 Aalto, Finland*
- ¹³⁶*Aalto University Metsähovi Radio Observatory, Metsähovintie 114, FI-02540 Kylmäla, Finland*
- ¹³⁷*Jeremiah Horrocks Institute, University of Central Lancashire, Preston PR1 2HE, UK*
- ¹³⁸*National Biomedical Imaging Center, Peking University, Beijing 100871, People's Republic of China*
- ¹³⁹*College of Future Technology, Peking University, Beijing 100871, People's Republic of China*
- ¹⁴⁰*Tokyo Electron Technology Solutions Limited, 52 Matsunagane, Iwayado, Esashi, Oshu, Iwate 023-1101, Japan*
- ¹⁴¹*Department of Physics and Astronomy, University of Lethbridge, Lethbridge, Alberta T1K 3M4, Canada*
- ¹⁴²*Frontier Research Institute for Interdisciplinary Sciences, Tohoku University, Sendai 980-8578, Japan*
- ¹⁴³*Astronomical Institute, Tohoku University, Sendai 980-8578, Japan*
- ¹⁴⁴*Department of Physics and Astronomy, Seoul National University, Gwanak-gu, Seoul 08826, Republic of Korea*
- ¹⁴⁵*University of New Mexico, Department of Physics and Astronomy, Albuquerque, NM 87131, USA*
- ¹⁴⁶*Physics Department, Brandeis University, 415 South Street, Waltham, MA 02453, USA*
- ¹⁴⁷*Tuorla Observatory, Department of Physics and Astronomy, University of Turku, Finland*
- ¹⁴⁸*Radboud Excellence Fellow of Radboud University, Nijmegen, The Netherlands*
- ¹⁴⁹*School of Natural Sciences, Institute for Advanced Study, 1 Einstein Drive, Princeton, NJ 08540, USA*
- ¹⁵⁰*School of Physics, Huazhong University of Science and Technology, Wuhan, Hubei, 430074, People's Republic of China*
- ¹⁵¹*Mullard Space Science Laboratory, University College London, Holmbury St. Mary, Dorking, Surrey, RH5 6NT, UK*
- ¹⁵²*Center for Astronomy and Astrophysics and Department of Physics, Fudan University, Shanghai 200438, People's Republic of China*
- ¹⁵³*Astronomy Department, University of Science and Technology of China, Hefei 230026, People's Republic of China*
- ¹⁵⁴*Department of Physics and Astronomy, Michigan State University, 567 Wilson Rd, East Lansing, MI 48824, USA*

ABSTRACT

The first very long baseline interferometry (VLBI) detections at 870 μm wavelength (345 GHz frequency) are reported, achieving the highest diffraction-limited angular resolution yet obtained from the surface of the Earth, and the highest-frequency example of the VLBI technique to date. These include strong detections for multiple sources observed on inter-continental baselines between telescopes in Chile, Hawaii, and Spain, obtained during observations in October 2018. The longest-baseline detections approach 11 G λ corresponding to an angular resolution, or fringe spacing, of 19 μas . The Allan deviation of the visibility phase at 870 μm is comparable to that at 1.3 mm on the relevant integration time scales between 2 and 100 s. The detections confirm that the sensitivity and signal chain stability of stations in the Event Horizon Telescope (EHT) array are suitable for VLBI observations at 870 μm . Operation at this short wavelength, combined with anticipated enhancements of the EHT, will lead to a unique high angular resolution instrument for black hole studies, capable of resolving the event horizons of supermassive black holes in both space and time.

Keywords: Very long baseline interferometry (1769); Radio interferometry (1346); Black holes (162); Supermassive black holes (1663); High angular resolution (2167); Astronomical techniques (1684); Event horizons (479)

1. INTRODUCTION

The technique of very long baseline interferometry (VLBI) involves a network of independently clocked telescopes separated by large distances, which simultaneously observe a common astronomical source (Thompson et al. 2017). The angular resolution, or fringe spacing, in a VLBI observation scales inversely with both the distance between stations (*i.e.*, the length of the baseline) and the observing frequency. The present article reports the first fringe detections made at 870 μm wavelength (345 GHz nominal frequency), which constitutes the shortest wavelength VLBI observation to date. The experiment we describe was intended as a first technical demonstration of the 870 μm VLBI capability using facilities that are part of the Event Horizon Telescope (EHT) array. Figure 1 shows the stations that participated in the fringe test along with the usual metric used to characterize mm-wavelength observing conditions: the 225 GHz zenith opacity (Thompson et al. 2017).

VLBI observing wavelength has decreased over time. The first 3 mm VLBI detections (at 86 GHz) were obtained through observations performed in 1981 (Readhead et al. 1983); the first 3 mm intercontinental detections (100 GHz) were obtained through observations performed in 1988 (Baath et al. 1991, 1992), and the first successful 1.3 mm (230 GHz) VLBI was carried out in 1989 (Padin et al. 1990). The especially long time since the last significant decrease in VLBI wavelength reflects the challenges of carrying out such observations, which are detailed below. Even so, there have been several milestones of note since the early 1990s on the path towards developing short wavelength VLBI as an important technique for astrophysics. Increased sensitivity through the use of larger telescopes and advanced receivers led to 1.4 mm (215 GHz) detections on a ~ 1100 km baseline of multiple active galactic nuclei (AGN) and Sagittarius A* (Sgr A*), the Galactic Center supermassive black hole (Greve et al. 1995; Krichbaum et al. 1997, 1998). A return to the longer-wavelength 2 mm spectral windows (147 GHz and 129 GHz) allowed extension of mm-wavelength VLBI to intercontinental baselines (Greve et al. 2002; Krichbaum et al. 2002; Doeleman et al. 2002). Building on this work, Doeleman et al. (2008, 2012) used purpose-built wideband digital VLBI systems on 1.3 mm trans-oceanic baselines to report the discovery of event-horizon scale structures in Sgr A* and the much more massive black hole, M87*. The Event Horizon Telescope (EHT) collaboration has now imaged both of these sources with a global 1.3 mm VLBI array (Event Horizon Telescope Collaboration et al. 2019a, 2022a, 2024).

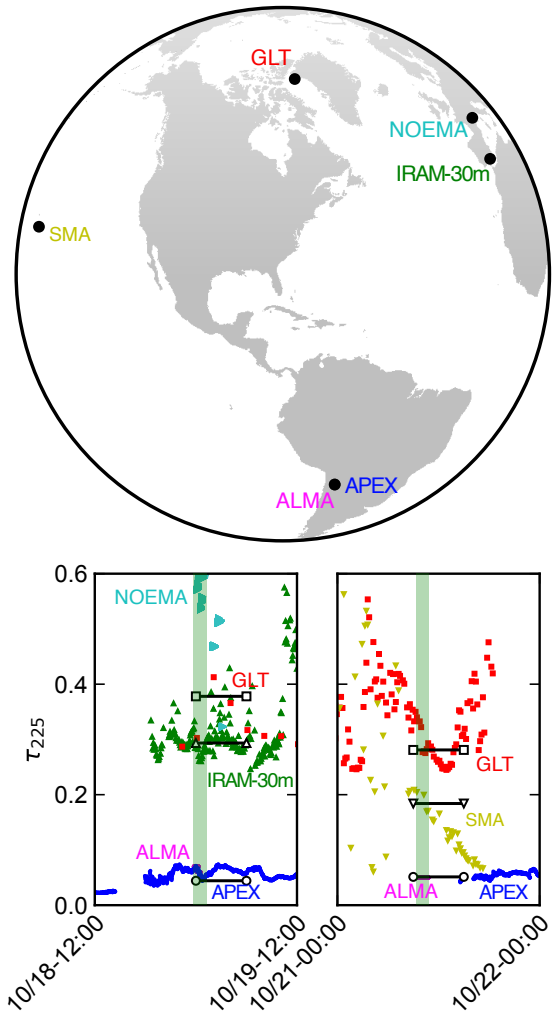


Figure 1. (top) Stations in the 870 μm fringe test. (bottom) Zenith opacity at 225 GHz, which is the standard frequency used for monitoring mm-wave conditions. The observing window on each day is indicated by the green shading. Conditions at ALMA were very good during both days ($\tau_{225} \approx 0.05$). The black lines indicate the opacity at each site calculated using inputs from MERRA-2 reanalysis during the observing windows, which we use to estimate 870 μm (345 GHz) opacity. Opacities for APEX and NOEMA have been estimated by converting precipitable water vapor column amounts.

The EHT is the highest-resolution ground-based VLBI instrument to date (Event Horizon Telescope Collaboration et al. 2019b). The EHT fringe spacing is approximately $25 \mu\text{as}$ at 1.3 mm wavelength. The finite diameter of the Earth limits ground-based 1.3 mm fringe spacing to $21 \mu\text{as}$ corresponding to $9.8 G\lambda$ baseline. In practice, modern imaging methods, such as regularized maximum likelihood,

* Corresponding Author: S. S. Doeleman, sdoeleman@cfa.harvard.edu

achieve a slightly higher angular resolution that exceeds the diffraction limit (Event Horizon Telescope Collaboration et al. 2019c).

For future campaigns, the EHT has developed the capability to observe at $870\ \mu\text{m}$, and enhancing the ability to observe at this wavelength through new stations and wider bandwidth is an important aspect of long-term enhancements envisaged by the next-generation EHT (ngEHT) project (Doeleman et al. 2019; Raymond et al. 2021; Doeleman et al. 2023). For a given set of station locations, observing at $870\ \mu\text{m}$ improves angular resolution by approximately 50% compared to observing at 1.3 mm, which will provide a sharper view of the black hole shadow and environment; the $870\ \mu\text{m}$ fringe spacing limit set by the diameter of the Earth is approximately $14\ \mu\text{as}$ corresponding to $14.7\ \text{G}\lambda$ baseline. Observations at $870\ \mu\text{m}$ are also important for polarimetric measurements. Faraday rotation, which scrambles the imaged electric field vector position angle pattern, diminishes with the square of the frequency. Therefore, $870\ \mu\text{m}$ observations may help distinguish Faraday rotation from the intrinsic field pattern set by the horizon-scale magnetic field and plasma properties (Event Horizon Telescope Collaboration et al. 2021; Wielgus et al. 2024). For Sgr A*, the angular size of the black hole shadow is larger than that of M87* (Event Horizon Telescope Collaboration et al. 2022a), but scattering in the ionized interstellar medium affects the image angular resolution (see, e.g., Johnson et al. 2018). At 1.3 mm, the scatter-broadening is comparable to the current EHT resolution, but it decreases approximately as the observing wavelength squared. Thus, at $870\ \mu\text{m}$, scattering effects would be significantly diminished and would not limit the resolution of a VLBI array for studies of Sgr A*. In particular, extension of the EHT to $870\ \mu\text{m}$ wavelengths can target photon ring substructure in Sgr A*, aiming to detect the orbit of light that makes a full “u-turn” around the black hole (Johnson et al. 2020; Palumbo et al. 2023). For these reasons, $870\ \mu\text{m}$ VLBI opens important new directions for advanced horizon-resolved studies of the two primary EHT sources. At the same time, higher frequency VLBI brings more sources into range for horizon-resolved black hole studies (Pesce et al. 2021; Ramakrishnan et al. 2023; Lo et al. 2023), and the increased resolution at $870\ \mu\text{m}$ benefits non-horizon VLBI studies of active galactic nuclei (AGN) jets (e.g., Kim et al. 2020; Janssen et al. 2021; Issaoun et al. 2022; Jorstad et al. 2023; Paraschos et al. 2024). Additionally, due to reduced opacity, shorter wavelengths probe more compact regions of jetted AGN sources (an example being the core-shift effect: Lobanov 1998; Hada et al. 2011). Hence, $870\ \mu\text{m}$ VLBI has the potential to image the jet launching region closer to the central black hole, enabling investigations of the physics behind jet formation, collimation, and acceleration. In particular, the poorly understood limb-brightening in transversely resolved inner jets (e.g. Janssen et al. 2021) can be studied in much greater detail.

Extension of observing to $870\ \mu\text{m}$ similarly enhances the capability of the EHT to capture dynamics near the event horizon. In the case of Sgr A*, the dynamical time scale

is $\sim 200\text{s}$ ($10GM/c^3$). Simultaneous 1.3 mm and $870\ \mu\text{m}$ observing can sample sufficient Fourier spatial frequencies within this integration time to allow snapshot imaging using the technique of multi-frequency synthesis (MFS; Chael et al. 2023). Combining such snapshots will enable recovery of accretion and jet launching kinematics. For M87*, the dynamical time scale is ~ 3 days, and data obtained in both 1.3 mm and $870\ \mu\text{m}$ on sequential days can be combined to form high-fidelity MFS images for time-lapse movie reconstruction of the event horizon environment. Realizing the full scientific potential of $870\ \mu\text{m}$ VLBI (Johnson et al. 2023) will require the planned ngEHT upgrade (Doeleman et al. 2023).

While there are clearly many motivating reasons for $870\ \mu\text{m}$ VLBI observing, a number of factors make the measurements difficult in this short-wavelength regime. The atmosphere is more opaque at $870\ \mu\text{m}$ than at 1.3 mm (see for example Liebe (1985); Matsushita et al. (1999); Matsushita et al. (2016); Matsushita et al. (2022)), which means that sources are more attenuated and noise levels due to atmospheric emission are elevated. Overall, the effective system temperatures of coherent radio receivers are intrinsically greater at $870\ \mu\text{m}$ than at 1.3 mm¹. The aperture efficiency of the collecting optics tends to diminish at high frequency, and the source flux density tends to decrease. In addition, coherence losses due to the VLBI frequency standards used at each site increase with observing frequency (Doeleman et al. 2011). The EHT array, conceived as a common, international effort of independent observatories working in the short millimeter range, has directly addressed these challenges and provides key enabling infrastructure for extension of VLBI to higher frequencies (Event Horizon Telescope Collaboration et al. 2019b).

The telescopes comprising the EHT array are precision structures sited at high-altitude, low-opacity locations (see e.g. Levy et al. (1996), Mangum et al. (2006), Greve & Bremer (2010), Chen et al. (2023) and references therein on the design and qualification of such instruments). State of the art instrumentation underpinning the operation of these telescopes, as single-dish facilities and for VLBI, includes cryogenic receivers and wideband digital backends - all refined over many years to optimize performance at mm and submm wavelengths. Steady improvements in superconductor-insulator-superconductor (SIS) junctions have formed the basis for increased bandwidth and sensitivity of mm and submm receivers, leading to state-of-the-art systems in use at EHT sites (see Maier et al. (2005), Tong et al. (2005), Chenu et al. (2007), Carter et al. (2012), Maier et al. (2012), Mahieu et al. (2012), Tong et al. (2013), Kerr et al. (2014), Chenu et al. (2016), Klein et al. (2014), Han et al. (2018), Belitsky et al. (2018)).

Following the successful 1.3 mm VLBI observations in 2017, test observations at $870\ \mu\text{m}$ were conducted on the

¹ See, for example, Janssen, M. et al. (2019) or ALMA Cycle 8 2021 Technical Handbook.

EHT array in October 2018. Conditions at the ALMA station during this test, including characterization of the system used there to phase the array for VLBI, are described in [Crew et al. \(2023\)](#). The present paper describes the VLBI test observations

2. METHODS

2.1. Schedule

The 870 μm fringe test observations consisted of two short scheduling blocks designed for two different subarrays. An eastern subarray, comprising ALMA, the Atacama Pathfinder EXperiment (APEX), Greenland Telescope (GLT), the Institut de Radioastronomie Millimétrique 30 m telescope (IRAM30m), and the Northern Extended Millimeter Array (NOEMA), was scheduled to include blazar sources that were visible in the nighttime hours at all sites: CTA 102, 3C 454.3, and BL Lac. A western subarray, comprising ALMA, APEX, GLT, and the Submillimeter Array (SMA), observed quasars J0423–0120, J0510+1800, J0521+1638, and J0522–3627. The eastern subarray scheduling block was followed by several scans on BL Lac at 1.3 mm wavelength to aid diagnosis in the event of a null result. Schedule blocks for both subarrays were optimized for fringe detection at 870 μm VLBI, and they spanned a duration of between 1 and 2 hours with at least two scans on every source. Most scans lasted five minutes.

The observing window consisted of five nights 2018 October 17–21 between approximately midnight and 2:00 Coordinated Universal Time (UTC) for the eastern subarray scheduling block and between 9:00 and 11:00 UTC for the western subarray scheduling block. Each scheduling block was triggered twice within the observing window. We report herein on successful observations with the eastern array on 2018 October 18–19 and with the western array on 2018 October 21. Details of the scheduling blocks and sources observed are shown in Fig. 2.

2.2. Instrumentation and Array

Several important technologies developed for 1.3 mm VLBI are leveraged to address the challenges of 870 μm observing, many of which are outlined in [Event Horizon Telescope Collaboration et al. \(2019b\)](#). The VLBI backends, used to condition and digitize signals from the telescope receivers, have a cumulative data rate of 64 Gbps ([Vertatschitsch et al. 2015](#); [Tuccari et al. 2017](#)) across four 2-GHz wide bands and two polarizations. Each station is outfitted with a hydrogen maser time standard, which had previously been found to be sufficiently stable for timekeeping in a 1.3 mm VLBI experiment and were expected to be sufficiently stable for 870 μm .

Phased array beamforming capability is implemented at both the SMA ([Young et al. 2016](#)) and ALMA ([Matthews et al. 2018](#)) array stations. For both these stations beamformer phasing efficiency at 870 μm , which directly scales the visibility amplitudes measured on baselines to the station, varied from just below 50% to as high as about 80%. These efficiencies are less than what is typical for 1.3 mm ([Event Horizon Telescope Collaboration et al. 2019b](#)). Section

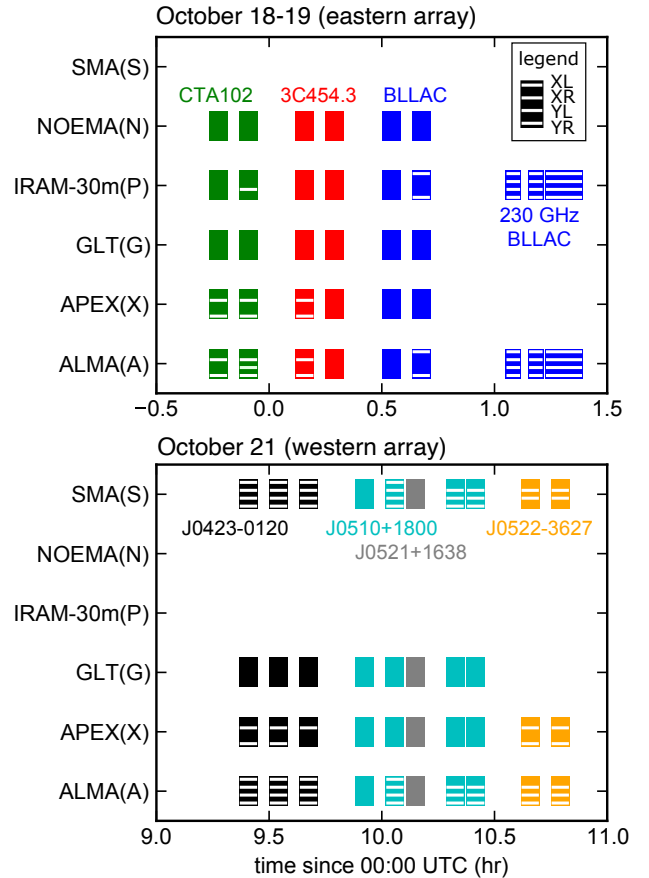


Figure 2. 870 μm observations that yielded detections were made during two separate scheduling blocks: October 18/19 and October 21, 2018. The observations on the first night were done with an eastern array comprising ALMA, APEX, GLT, IRAM30m, and NOEMA. Observations on the second night were made with a western array: ALMA, APEX, GLT, and SMA. The scheduling blocks for both nights are shown along with the one-letter station codes, which are listed in parenthesis. All detections are on baselines involving ALMA. The scans which yielded detections on baselines defined by a given station are indicated by the white horizontal ticks centered in each time block: from the top, ticks correspond to XL, XR, YL, YR mixed-polarizations per the legend shown upper right. The absence of a tick indicates a non-detection. Three scans at 230 GHz (1.3 mm) were performed at the end of the eastern subarray scheduling block using just the IRAM30m and ALMA facilities.

3.4 has discussion relevant to ALMA, SMA, and also to NOEMA² of phasing efficiency challenges and planned improvements to mitigate these.

The frequency setup for the 870 μm fringe test is similar to that described in Table 4 of [Event Horizon Telescope Collaboration et al. \(2019b\)](#). Most stations in the array ob-

² NOEMA is also equipped with the phased array though it was not commissioned at the time of this observation.

served a single 2048 MHz band at a 4–6 GHz intermediate frequency (IF) using a 342.6 GHz sky local oscillator (LO)³. That frequency setup corresponds to a sky frequency range of 346.552 to 348.6 GHz. Each station observed both circular polarizations, with the exceptions of APEX (right-circular polarization, RCP, only) and ALMA (dual linear, X and Y). The recorded station data were correlated using DiFX software (Deller et al. 2011) at the MIT Haystack Observatory. Visibility data on baselines to ALMA remained in a mixed-polarization basis (*i.e.*, $\{X,Y\} \times \{L,R\}$) because the observing schedules were not long enough to track polarization calibrators over a wide range of parallactic angle, which is necessary for converting the ALMA data from a linear to circular basis (Martí-Vidal et al. 2016; Matthews et al. 2018; Goddi et al. 2019). Subsequent fringe fitting was done using the Haystack Observatory Post-processing System (HOPS⁴, Whitney et al. (2004); see also Blackburn et al. (2019)).

2.2.1. ALMA

ALMA observed in dual linear polarization with IRAM designed 870 μm (*i.e.*, Band 7) cartridges (Mahieu et al. 2012). The ALMA Phasing System (APS) (Matthews et al. 2018) was used to aggregate the collecting area of the active dishes in the ALMA array. The APS capability had been used previously for VLBI science at 3 mm (Issaoun et al. 2019; Okino et al. 2022; Zhao et al. 2022) and 1.3 mm (Event Horizon Telescope Collaboration et al. 2019a,b) but not at shorter wavelengths albeit that setup for 870 μm observations is similar to the longer wavelength bands. In the 870 μm experiment, the four recorded 2.048 GHz subbands were tuned to center frequencies of 335.6, 337.541406, 347.6 and 349.6 GHz. The choice of the 337.541406 GHz frequency results from ALMA-specific tuning restrictions.

The ALMA phased array included twenty-five 12 m antennas during the eastern track and twenty-nine 12 m antennas during the western track with a maximum antenna spacing of 600 m in both cases. Wind speeds were greater than 10 m s⁻¹ at the ALMA site. During the Eastern track, phasing efficiency was below 50% for most of the time and at best was about 80%. During the October 21 track (western) in better weather, phasing efficiency was more stable and greater than approximately 90% (Crew et al. 2023).

2.2.2. APEX

The APEX and ALMA stations are co-located and conditions were similar at the two telescopes. APEX observed using the 345 GHz FLASH+ linear receiver (Klein et al. 2014). That receiver may not have been functioning optimally during the experiment and has since been replaced by the Swedish-ESO PI Instrument for APEX (SEPIA) (Belitsky et al. 2018; Meledin, D. et al. 2022). A quarter wave

plate was used to achieve circular polarization. Two backends, a ROACH2 Digital Backend (R2DBE; Vertatschitsch et al. 2015) and a Digital BaseBand Converter 3 (DBBC3; Tuccari et al. 2017), were operated in parallel.

2.2.3. GLT

The GLT station participated in the observation but at the time was still commissioning specific subsystems. The GLT antenna has operated at Pituffik Space Base, formerly the Thule Airbase site, in Greenland since August 2017 (Inoue et al. 2014; Raffin et al. 2016; Matsushita et al. 2018; Koay et al. 2020; Chen et al. 2023). The GLT observed in dual linear polarization with the IRAM-made 870 μm (*i.e.*, Band 7) cartridges (Mahieu et al. 2012). The 345 GHz receiver on the GLT saw first-light in continuum and spectral-line modes in August 2018. Pointing and focus calibration at 345 GHz were still in the commissioning phase during the 870 μm observation reported here. The GLT pointing system has since been fully commissioned for recent and future VLBI observing. Similarly, final adjustments to the dish surface had yet to be made, and the surface accuracy was estimated to be 170 μm rms during the observations reported here. Subsequent improvements have led to rms surface accuracy in the 17-40 μm range (see Table 7 in Chen et al. (2023)).

2.2.4. IRAM30m

The IRAM30m telescope used the heterodyne Eight Mixer Receiver (Carter et al. 2012) in the 870 μm band also known as E330. The setup and pre-observing checks were analogous to a regular Global Millimeter VLBI Array or EHT session. The opacity at 870 μm during the scheduled VLBI observations was high and would not typically have triggered single-dish science operation at this wavelength.

2.2.5. NOEMA

Portions of the NOEMA station were still being commissioned during the 870 μm experiment. NOEMA observed in dual polarization as a single-antenna station not as a phased array. The NOEMA receiver was a dual-polarization single-sideband unit (Chenu et al. 2016) with a 4 GHz bandpass. Recording was with a 16 Gbps R2DBE backend. The NOEMA phased array has since been commissioned for VLBI observing.

2.2.6. SMA

The SMA station observed with seven antennas arranged in the compact configuration with a maximum baseline of 69.1 m. The SMA Wideband Astronomical ROACH2 Machine (SWARM) (Primiani et al. 2016; Young et al. 2016) was run with the VLBI beamformer mode activated producing a coherent phased array sum of the seven antennas, formatted for VLBI recording. As expected the phasing efficiency was lower than for 1.3 mm operations. The sky LO was set to 341.6 GHz, not 342.6 GHz, to match the SWARM sky coverage with the other stations, compensating for a different IF to baseband local oscillator because

³ ALMA and SMA used slightly different frequency setups to match the sky frequency of the other stations, see sections 2.2.1 and 2.2.6.

⁴ <https://www.haystack.mit.edu/tech/vlbi/hops.html>

SWARM uses its own block downconverter rather than the standard EHT single dish equipment. The data were recorded in the frequency domain at the standard SMA clock rate (4.576 Gsps) which differs from the standard EHT single dish sample rate of 4.096 Gsps (Vertatschitsch et al. 2015). APHIDS (Adaptive Phased Array Interpolating Downsampler for SWARM) post-processing was completed to interpolate and invert (from frequency- to time-domain) the SWARM data sets in preparation for VLBI correlation. After APHIDS processing the SMA EHT data product matches that produced by standard SMA single dish station in sample rate, and is also a time series matching the standard EHT single dish data product.

3. RESULTS AND DISCUSSION

Figure 1 shows that the conditions during the experiment were mixed across the array. While the observatories do not measure 870 μm (345 GHz) opacity directly, we use MERRA-2 reanalysis and radiative transfer (Paine 2022) that is validated by measurements at 225 GHz (Fig. 1 black lines) to estimate τ_{345} . For the eastern subarray on October 18/19, τ_{345} was 0.2 at the ALMA and APEX sites, and 0.8 at IRAM30m. For the western subarray on October 21, τ_{345} was approximately 0.17 at the ALMA and APEX sites and 0.7 at SMA. During the experiment, the opacities at GLT and NOEMA were unfavorable and detections on baselines to those stations were not achieved; however, both stations have weather that is compatible with 870 μm observing and will likely yield high-frequency detections in the future (see e.g., Raymond et al. (2021); Matsushita et al. (2022)). Atmospheric conditions can change rapidly: τ_{225} at the SMA decreased by nearly a factor of four in the hours following the experiment.

3.1. 870 μm (345 GHz) Fringes

In VLBI, recorded data from all sites are brought to a central processing facility where data streams from each pair of sites are cross-correlated. The resulting complex correlation quantities provide a dimensionless measure of the electric field coherence between the two sites, which is proportional to a Fourier component of the brightness distribution of the target source. The correlation processor uses an apriori model to align the site data streams, recreating the exact geometry of the physical baseline connecting the two sites at the time of observation. Because the apriori model is imperfect, after processing the cross correlation phase typically varies as a function of time and frequency due to residual delay and delay-rate respectively. To average the correlation signal over frequency and time, the correlator output is thus searched over a range of delay and delay-rate to find a peak in correlator power - a process also known as ‘fringe-fitting’ (Thompson et al. 2017). In this experiment, the correlator output was searched by dividing each scan into short segments and incoherently averaging them. The incoherent averaging technique (Rogers et al. 1995) estimates noise-debiased VLBI quantities, and it is well suited to processing low- S/N VLBI data on sparse arrays as it allows integration beyond the nom-

inal atmospheric coherence time. Figure 3 shows the dependence of amplitude in units of 10^4 and signal-to-noise ratio (S/N) on the duration of the segments for a sample scan on source J0423–0120 for the baseline comprising the ALMA and SMA stations. All four cross-hand polarizations are plotted. The scan identifier 294-0938 in Fig. 3 corresponds to the *day-UTC* for the beginning of the scan, where the *day* is the number of days since January 1, 2018 (294 is October 21) and *UTC* is the scan start time. The noise-debiased amplitude (Rogers et al. 1995) in Fig. 3 is indicated by the dashed horizontal line. As the segment duration decreases, the effect of decoherence is reduced so the S/N increases.

Compared to a single coherent integration over a full scan (approximately 300 s in most of the measurements), incoherently averaging the parts of a segmented scan increases the S/N by up to a factor of two on many of the measurements, yielding higher confidence in the detections. For most of the measurements, S/N values asymptote at the shortest segment durations. Ordinarily, we would expect the S/N values to decrease as the segments are shortened below the coherence time. The behavior we observe could be indicative of a changing coherence during the scan consistent with the windy conditions at ALMA (Crew et al. 2023).

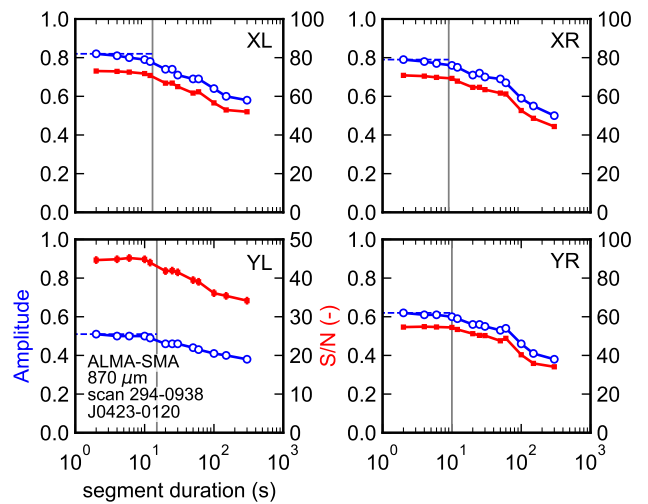


Figure 3. Scan averaged and noise-debiased 870 μm fringe amplitude (open blue circles, left axes) and S/N (closed red squares, right axes). Amplitudes and S/N are computed by first dividing each observing scan into short coherently integrated segments, which are then combined incoherently following the procedure in Rogers et al. (1995). Segment length is shown on the horizontal axis. Each subplot shows a different polarization on the ALMA-SMA baseline for a single scan on J0423–0120 (October 21, 09:38 UTC). Other detections listed in Table 1 have similar dependence on segment duration though generally lower S/N . The noise-debiased amplitude and coherence time were derived using HOPS and are indicated by the horizontal blue dashed line and the vertical solid black line, respectively.

Contours of fringe power versus multi-band delay and rate are plotted in Fig. 4 for a single scan of J0423–0120 on the ALMA-SMA baseline. The measurement exhibits a definitive peak in fringe power for each of the cross-hand polarizations. The rates are all centered near zero. Multi-band delays fall within an ambiguity search window of (-8.53 ns, 8.53 ns) as they are derived from measurements spaced at ALMA’s channel separation of 58.592375 MHz (Matthews et al. (2018); Event Horizon Telescope Collaboration et al. (2019d)).

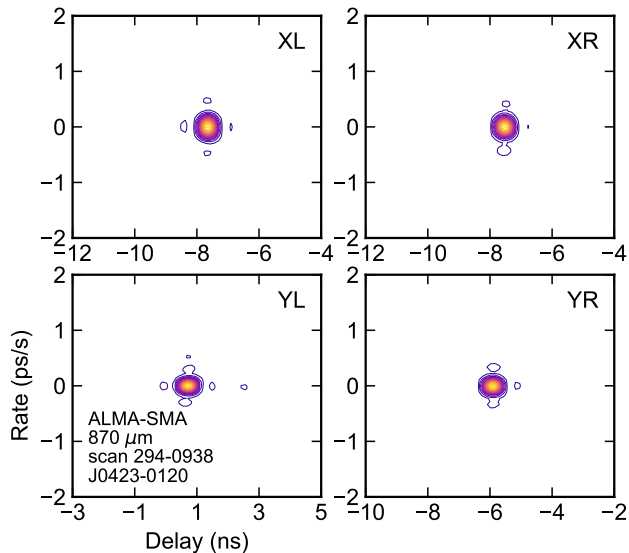


Figure 4. 870 μm contours of incoherently-averaged fringe power in 5% increments versus delay and rate for a single scan on J0423–0120 for the ALMA-SMA baseline (October 21, 09:38 UTC). Other detections reported in Table 1 also exhibit clear peaks versus delay/rate.

The fringe detection threshold was conservatively set at $S/N > 7$ to prevent false detections, and all resulting detections are summarized in Table 1 ordered by target source. The maximum spatial frequencies sampled are greater than $10.9 \text{ G}\lambda$ between ALMA and the SMA, which significantly exceeds the largest spatial frequencies sampled by the EHT for M87* at 1.3 mm on the longest baseline between Hawaii and Europe (approximately $8 \text{ G}\lambda$). The highest S/N detections exceed 70. Simultaneous detections in all four polarization products were achieved on the ALMA-SMA baseline for J0423–0120. The zero-baseline flux densities at 870 μm were obtained from the ALMA local interferometry (Crew et al. 2023). The flux densities were 1.4, 1.0, 2.4, 1.2, and 4.9 Jy on CTA 102, BL Lac, J0423–0120, J0510+1800, and J0522–3627, respectively. The source structure of the targets in this work is not known a priori, so it is not possible to say with precision how the correlated amplitudes should vary as a function of baseline length. Furthermore, these observations were designed to be a detection experiment, and not carried out with all procedures that would allow robust VLBI flux

density calibration. Nevertheless, the SNR on the ALMA-APEX baselines appears to be anomalously low given the short baseline length, which would ordinarily be sensitive to both small scale structure (10–100 μas) and larger scale structure (10–100 mas). This is likely attributable to phase instabilities suspected in the APEX receiver (see Section 2.2.2), which has since been retired. Follow-on experiments, already scheduled, will focus on calibration and robust flux density measurements vs. baseline length.

HOPS reports two coherence times: one corresponding to the point below which there is only a small amount of coherence loss within the uncertainty of amplitudes and another corresponding to the maximum S/N . For most of the scans in Table 1, we report the former. In a few low- S/N cases where the routine was unable to fit the coherence, the coherence time based on S/N is reported instead. The coherence times across baselines range from approximately ten to thirty seconds for most cases. For BL Lac, the longer coherence times may be an artifact of the moderate S/N .

3.2. 1.3 mm (230 GHz) Comparison

Presently, the EHT observes at 1.3 mm (Event Horizon Telescope Collaboration et al. 2019b). Figure 5 compares the Fourier components of the 870 μm detections on various sources to the 1.3 mm coverage of the 2017 EHT array on M87* (Event Horizon Telescope Collaboration et al. 2019d). The 870 μm detections on ALMA-IRAM30m and ALMA-SMA baselines have a higher nominal angular resolution (19 μas) than the highest-resolution M87* detections (nominally 25 μas).

For a source-specific comparison of the 1.3 mm and 870 μm bands, ALMA and IRAM30m observed BL Lac at 1.3 mm during three scans at the end of the eastern subarray scheduling block of the October 2018 session. Those data were searched using the same HOPS incoherent averaging method as was used for the 870 μm observations and provide an independent application of the approach. The 1.3 mm scans provide a check of the 870 μm processing and a point of comparison for the 870 μm detections.

The amplitude and S/N values for one of the 1.3 mm scans are plotted in Fig. 6 versus the duration of incoherently-averaged segments. The S/N values are approximately 10-fold greater at 1.3 mm than at 870 μm (see Figure 3), which likely results from a combination of factors that boost sensitivity at the longer wavelength: lower opacity, lower receiver noise, greater aperture efficiency, a wider beam, greater coherence, and greater source flux density. The coherence time determined using HOPS was comparable for the three scans to what was found at 870 μm : on the order of 6 to 30 seconds. As with the 870 μm measurements, the S/N values asymptote as the segment duration decreases below the coherence time. The consistency of the S/N trends in the 870 μm and 1.3 mm scans suggests that the behavior is a real feature of the data and not an artifact of the analysis.

Comparison of the 1.3 mm and 870 μm wavelengths observing BL Lac also shows that the latter is a much more difficult regime in which to operate. The atmospheric con-

Table 1. 870 μm detections on the indicated baselines, sources, and polarizations.

Baseline [†]	Pol.	Day*	Time (hh:ss)	El. 1 (°)	El. 2 (°)	$ \bar{u}-\bar{v} $ (G λ)	τ_c (s)	Delay (ns)	Rate (fs s ⁻¹)	Amp. ($\times 10^{-4}$)	S/N
3C 454.3											
AX	XR	292	00:07	44.9	45.0	0.0026	8	4.4	-1	0.50	43.7
AX	YR	292	00:07	44.9	45.0	0.0026	8	5.2	-1	0.47	41.4
BL Lac											
AP	XL	292	00:38	24.6	42.6	9.7913	31	-4.6	4	0.15	12.2
AP	YR	292	00:38	24.6	42.6	9.7913	46	-8.5	0	0.13	10.8
CTA 102											
AP	YL	291	23:52	49.7	43.5	9.9581	21	0.9	-38	0.18	13.6
AX	XR	291	23:44	48.6	48.7	0.0027	24	5.6	-38	0.23	19.2
AX	XR	291	23:52	49.7	49.7	0.0027	10	5.2	-85	0.23	20.8
AX	YR	291	23:44	48.6	48.7	0.0027	22	6.3	-51	0.21	17.6
AX	YR	291	23:52	49.7	49.7	0.0027	11	6.0	-84	0.22	18.0
J0423-0120											
AS	XL	294	09:22	48.5	35.5	10.8547	14	-7.6	6	0.54	47.8
AS	XL	294	09:30	46.8	37.3	10.8874	14	-8.0	0	0.70	62.4
AS	XL	294	09:38	45.1	39.1	10.9100	13	-7.7	-2	0.82	73.1
AS	XR	294	09:22	48.5	35.5	10.8547	9	-7.5	19	0.60	53.4
AS	XR	294	09:30	46.8	37.3	10.8874	34	-7.9	-0	0.64	56.6
AS	XR	294	09:38	45.1	39.1	10.9100	9	-7.5	-2	0.79	70.8
AS	YL	294	09:22	48.5	35.5	10.8547	13	0.8	19	0.34	29.6
AS	YL	294	09:30	46.8	37.3	10.8874	17	0.4	0	0.47	41.3
AS	YL	294	09:38	45.1	39.1	10.9100	15	0.7	-2	0.51	45.2
AS	YR	294	09:22	48.5	35.5	10.8547	10	-5.9	19	0.46	40.7
AS	YR	294	09:30	46.8	37.3	10.8874	14	-6.3	0	0.50	44.2
AS	YR	294	09:38	45.1	39.1	10.9100	10	-5.9	-3	0.62	54.9
AX	XR	294	09:22	48.5	48.5	0.0028	27	-1.0	-8	0.14	12.6
AX	XR	294	09:30	46.8	46.8	0.0028	39	-0.9	-9	0.16	13.0
AX	XR	294	09:38	45.1	45.1	0.0028	32	-0.9	-11	0.15	12.9
AX	YR	294	09:22	48.5	48.5	0.0028	30	0.6	-7	0.14	10.9
AX	YR	294	09:30	46.8	46.8	0.0028	29	0.7	-9	0.14	10.8
J0510+1800											
AS	XL	294	10:01	37.0	39.6	10.9218	30	-8.0	-12	0.10	8.5
AS	XR	294	10:01	37.0	39.6	10.9218	28	-8.0	-12	0.25	22.3
AS	XR	294	10:17	34.5	43.4	10.8891	8	-8.1	-0	0.27	22.4
AS	XR	294	10:22	33.5	44.8	10.8682	22	2.2	20	0.20	16.6
AS	YL	294	10:01	37.0	39.6	10.9218	10	0.3	-12	0.20	18.1
AS	YL	294	10:17	34.5	43.4	10.8891	23	0.2	11	0.25	21.3
AS	YL	294	10:22	33.5	44.8	10.8682	29	-6.6	2	0.17	14.2
AS	YR	294	10:01	37.0	39.6	10.9218	28	-6.3	-14	0.12	10.1
AS	YR	294	10:17	34.5	43.4	10.8891	6**	-6.5	0	0.14	11.5
AS	YR	294	10:22	33.5	44.8	10.8682	10**	3.8	81	0.11	9.7
J0522-3627											
AS	XR	294	10:37	53.0	18.0	10.3188	12**	-4.7	38	0.12	10.1
AS	XR	294	10:45	51.4	19.2	10.4084	24	-4.9	8	0.20	12.1
AS	YL	294	10:37	53.0	18.0	10.3188	29	3.5	-4	0.12	10.3
AS	YL	294	10:45	51.4	19.2	10.4084	22	3.4	-4	0.16	14.1
AX	XR	294	10:37	53.0	52.9	0.0030	31	0.8	-1	0.31	26.9
AX	XR	294	10:45	51.4	51.4	0.0030	39	0.8	25	0.25	15.3
AX	YR	294	10:37	53.0	52.9	0.0030	31	2.3	1	0.31	27.0
AX	YR	294	10:45	51.4	51.4	0.0030	31	2.4	25	0.29	24.6

[†] Baselines: AX (ALMA-APEX), AP (ALMA-IRAM30m), AS (ALMA-SMA)

* Day of Year in 2018.

**The S/N was insufficient to fit the coherence time. The reported value is the segmentation time that achieves the greatest S/N for the scan.

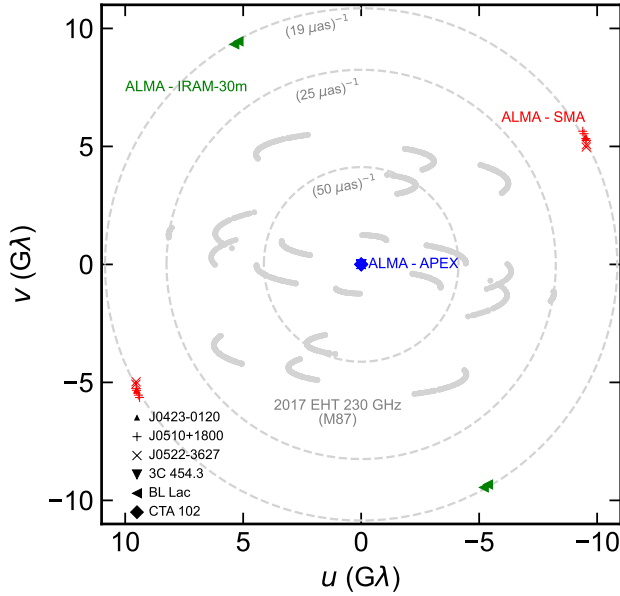


Figure 5. Detections on various targets at 345 GHz (see Table 1). The u - v locations of 230 GHz detections on M87* during the EHT April 2017 campaign are shown in gray including low- S/N scans at $(25\mu\text{as})^{-1}$.

ditions at the IRAM30m site (see Fig. 1; $\tau_{345} \sim 0.8$) were not ideal for $870\mu\text{m}$ observing during the test. At 1.3 mm, strong detections were obtained on all polarizations for each of the three attempted scans. At $870\mu\text{m}$, detections were made on just two of four polarizations for a single ALMA-IRAM30m scan, and none were made on other BL Lac baselines. The 10-fold greater S/N values at 1.3 mm are consistent with the system equivalent flux density (SEFD). The SEFD on BL Lac scans at ALMA were approximately 150 Jy at 1.3 mm versus 580 Jy at $870\mu\text{m}$ (factor of 3.9 change). At IRAM30m, SEFDs during the BL Lac scans were 3800 Jy at 1.3 mm versus 10^5 Jy at $870\mu\text{m}$ (factor of approximately 25 change). The S/N is inversely proportional to the root product of the SEFDs, or $\sqrt{3.9 \times 25} \approx 10$, which explains the behavior across observing wavelengths. The significantly greater noise at $870\mu\text{m}$ as well as the other losses associated with narrower beam width or coherence is the likely reason for non-detections to some stations and on certain scans.

Fringe power contours at 1.3 mm are plotted as a function of multi-band delay and rate in Fig. 7, exhibiting obvious peaks. The delays for each of the four polarization cross products is consistent across scans, and the 1.3 mm fringes are summarized in Table 2. All four polarization cross-hands are detected in each of the three 1.3 mm scans. The 6.4 Gλ spatial frequencies are 50% smaller than the $870\mu\text{m}$ scans on the AP baseline, which corresponds to the frequency scaling between the two bands. The 1.3 mm zero-baseline flux density of BL Lac deduced from the ALMA local interferometry (Crew et al. 2023) was 1.2 Jy.

3.3. Coherence and Allan Deviation

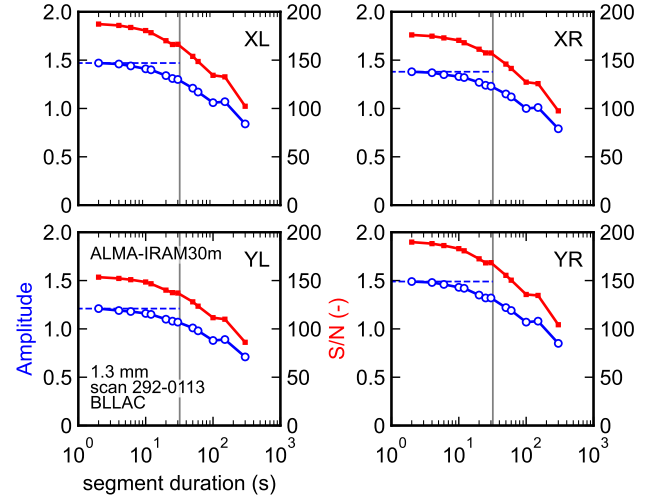


Figure 6. 1.3 mm amplitude (open blue circles, left axes) and S/N (closed red squares, right axes) versus the duration of coherently integrated segments, which are incoherently averaged. Each subplot shows a different polarization on the baseline between ALMA and IRAM30m for a single scan on BL Lac on October 19, 01:13 UTC. Other BL Lac detections listed in Table 2 have similar dependence on segment duration. The noise-debiased amplitude and coherence time were derived using HOPS and are indicated by the horizontal blue dashed line and the vertical solid black line, respectively. These data were calibrated in the same manner as the $870\mu\text{m}$ detections.

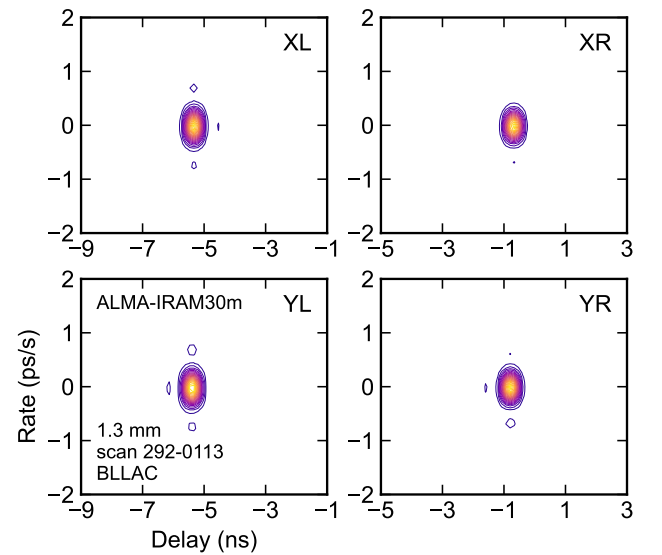


Figure 7. 1.3 mm contours of incoherently-averaged fringe power in 5% increments versus delay and rate for the baseline between ALMA and IRAM30m. This example is for a single scan on BL Lac taken on October 19, 01:13 UTC. Other detections reported in Table 2 also exhibit clear peaks versus in delay-delay rate search space.

It is convenient to characterize the phase noise of an interferometer by its Allan deviation, which is a measure of

Table 2. 1.3 mm detections on the ALMA – IRAM-30 m baseline toward BL Lac for indicated polarizations. Scans listed top to bottom on October 19 begin at 01:03, 01:09, and 01:13 UTC.

Elevation (ALMA/IRAM30m) ($^{\circ}$)	Baseline Length (G λ)	τ_c (s)	Delay (ns)	Rate (fs s $^{-1}$)	Amp. ($\times 10^{-4}$)	S/N
<i>XL</i>						
24.5 / 38.3	6.4327	5	-5.3	-98	1.66	134.0
24.4 / 37.3	6.4422	7	-5.3	-66	1.49	120.0
24.3 / 36.6	6.4476	32	-5.3	-14	1.47	187.3
<i>YR</i>						
24.5 / 38.3	6.4327	6	-0.8	-99	1.77	143.0
24.4 / 37.3	6.4422	7	-0.8	-66	1.52	122.4
24.3 / 36.6	6.4476	32	-0.8	-14	1.49	189.8
<i>XR</i>						
24.5 / 38.3	6.4327	6	-0.7	-98	1.56	125.4
24.4 / 37.3	6.4422	7	-0.7	-66	1.37	110.4
24.3 / 36.6	6.4476	32	-0.7	-13	1.38	176.1
<i>YL</i>						
24.5 / 38.3	6.4327	6	-5.4	-98	1.42	114.4
24.4 / 37.3	6.4422	7	-5.4	-66	1.24	100.1
24.3 / 36.6	6.4476	32	-5.4	-14	1.21	153.5

fractional stability for an oscillator, time standard or any time variable process. When computing the Allan deviation of observed VLBI interferometer phase one normalizes by the frequency of observation to produce a dimensionless quantity. The relationships of Allan deviation to the statistical variance, coherence, and phase power spectrum can be found in [Thompson et al. \(2017\)](#). Examples of the Allan deviation of VLBI systems referenced to hydrogen maser time standards and operating at 1.3 cm and 3 mm wavelength are can be found in [Rogers & Moran \(1981\)](#) and [Rogers et al. \(1984\)](#) respectively, and show that at short wavelengths decoherence is a potential concern. Alternatives to hydrogen masers for short-wavelength VLBI work have been explored (e.g., [Doeleman et al. \(2011\)](#)). In this section we compare the observed Allan deviation of the VLBI interferometric phase to limiting factors including the stability of time and frequency standards used in the experiment as well as instabilities due to atmospheric turbulence.

Figure 8 shows the Allan deviation for 870 μm scans on the ALMA-SMA baseline. Over most integration times, the 870 μm Allan deviation is comparable to but greater than the maser-maser reference. The 870 μm traces exhibit relatively small scan-to-scan variation during the course of the brief fringe test when conditions were relatively stable. For comparison, Fig. 8 also shows the Allan deviations for a large number of high-S/N 1.3 mm scans from the 2017 EHT campaign ([Event Horizon Telescope Collaboration et al. 2019d](#)). At times less than about 5 s, the red 1.3 mm traces all approach the limit set by the maser references. At times longer

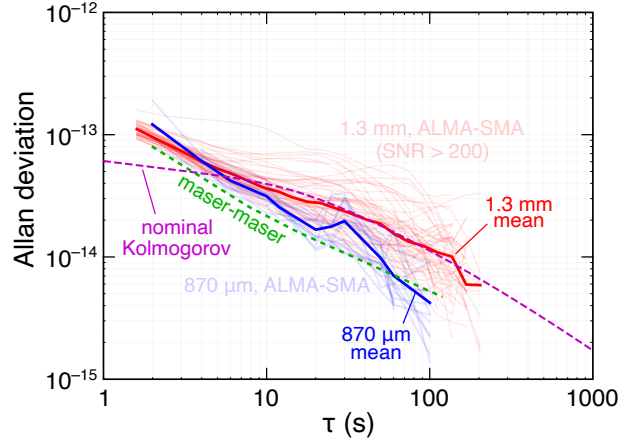


Figure 8. Allan deviation for 870 μm (345 GHz) scans observed on the ALMA-SMA baseline (blue traces). For comparison, red traces show the Allan deviation for high-S/N scans (nominally 5 minutes long) during the 1.3 mm (230 GHz) 2017 EHT campaign ([Event Horizon Telescope Collaboration et al. 2019b](#)). Weather variability during the 2017 campaign is responsible for the spread in those scans. The means of the individual Allan deviation traces are shown in bold for the two frequencies. The 870 μm and 1.3 mm mean traces approach the nominal Allan deviation for a pair of T4 Science brand iMaser 3000 model masers ([Thompson et al. 2017](#)) at short timescales. At intermediate timescales, atmospheric turbulence can become important. The Allan deviation associated with Kolmogorov turbulence is plotted for a set of nominal parameters ([Treuhaft & Lanyi 1987](#)).

than 5 s, the red traces are noticeably scattered. The scatter exists because of the variability of atmospheric conditions during the course of an observing campaign.

The tropospheric delay is essentially independent of wavelength for wavelengths longer than about 600 μm as described by the Smith-Weintraub equation (see [Thompson et al. \(2017\)](#), chapter 13). Thus the Allan deviation is expected to be independent of wavelength for our observations. When the atmospheric conditions are stable the 1.3 mm Allan deviation for individual scans approaches the maser-maser limit across all integration times. The mean of the 1.3 mm scans is within a factor of approximately two of the mean of the 870 μm traces. The 870 μm mean Allan deviation on the plot happens to be lower than the 1.3 mm mean for most integration times. However we do not consider this difference to be significant give the extremely small 870 μm data set. Further, the observations in 2017 April and 2018 October observations were of course made in differing weather conditions.

To assess the impact of atmospheric turbulence at longer times, the Allan deviation associated with atmospheric Kolmogorov turbulence is plotted for a set of nominal conditions following the approach outlined by [Treuhaft & Lanyi](#)

(1987): 10 m s^{-1} wind speed, 2 km troposphere scale height, $1.99 \times 10^{-7} \text{ m}^{-1/3}$ Kolmogorov coefficient, and independent distant sites. The nominal Kolmogorov trace exceeds the maser-maser Allan deviation at longer times where we expect atmospheric effects to dominate. Beyond 10 s, the nominal Kolmogorov trace matches the shape of the 1.3 mm mean. Although the $870 \mu\text{m}$ mean falls somewhere between the maser-maser and nominal Kolmogorov limits, the atmospheric contribution may become more apparent the future with scans spanning more variable weather conditions.

3.4. Phasing Efficiency

An important figure of merit when used to monitor the performance of phased array beamformers is phasing efficiency. This is a measure of how effectively outputs of the dishes in the local array are coherently summed to synthesize a single IF output from the array's aggregated collecting area. For each array site periodic estimates of phasing efficiency over time are stored with other essential metadata for use in calibration.

The ALMA and SMA phased arrays experienced lower and more variable phasing efficiency during the $870 \mu\text{m}$ test than is typical for 1.3 mm observing in similar conditions. At $870 \mu\text{m}$ atmospheric opacity is between 3 and 3.5 times that for 1.3 mm given the same precipitable water vapor (PWV). Further source fluxes decline with increasing frequency or shorter wavelength. Both of these factors result in lower local array fringe signal-to-noise-ratio (SNR). There is thus greater error in the fits of the antenna phase corrections. Tuning within the band avoids the deep absorption lines due to atmospheric water resonances at 325 and 385 GHz which would reduce the SNR still further. Also, the atmospheric phase fluctuations tracked by the adaptive phased array system have a greater amplitude for observations in the higher frequency band. Crew et al. (2023) note that that moist, windy conditions tend to diminish phasing efficiency, and the winds were quite high at ALMA during the test. At dry less windy times ALMA obtained higher phasing efficiencies approaching 100%. While NOEMA participated in this test with a single dish, not as a phased array, all of these factors are expected to apply as well to NOEMA which is now equipped with a phased array back end capable of beamforming in both the 1.3 mm and $870 \mu\text{m}$ bands.

Water vapor radiometer (WVR) based phasing corrections were not in use during the 2018 test. Independent testing at ALMA show that fast WVR corrections are effective at improving the efficiency when phase fluctuations are primarily due to water vapor. Phasing control loop algorithms are constantly being improved and in future will be better tuned to the $870 \mu\text{m}$ waveband. These improvements will expand the opportunities for $870 \mu\text{m}$ observing in a wider range of weather conditions and on weaker sources. Despite these challenges VLBI detections at $870 \mu\text{m}$ can be readily achieved even when phasing efficiencies are relatively low and in non-ideal weather conditions.

4. FUTURE DIRECTIONS

Achieving $870 \mu\text{m}$ VLBI fringes has strong implications for science directions that future global arrays operating at this wavelength can explore. As angular resolution scales with wavelength, we anticipate improving resolution from $\sim 23 \mu\text{as}$ to $\sim 15 \mu\text{as}$ on the longest EHT baselines (Figure 5). Plasma propagation processes typically scale as wavelength squared, so at $870 \mu\text{m}$ scatter broadening of Sgr A* reduces to $\sim 5 \mu\text{as}$, further sharpening resolution and increasing signal-to-noise on the longest VLBI baselines. Similarly, Faraday Rotation measured across the bandpass of EHT receivers at $870 \mu\text{m}$ can be used to improve estimates of accretion plasma densities and magnetic field geometries close to EHT targets. For both Sgr A* and M87* the images at $870 \mu\text{m}$ and 1.3 mm are determined predominantly by the achromatic gravitational lensing, and hence should exhibit similar characteristics, implying that the aggregate Fourier coverage of VLBI observations at different frequencies can be used to improve modeling of the gravitationally lensed emission, and imaging fidelity generally (Chael et al. 2023). Figure 9 shows Fourier amplitudes as a function of radius for GRMHD⁵ models of M87* and Sgr A*. Inclusion of 345 GHz observations adds coverage in the visibility plane regions not sampled at 230 GHz, and it extends baseline lengths for higher angular resolution as well as enhanced overall sampling of Fourier spatial frequencies to allow dynamical reconstructions of accretion and jet launch close to the event horizon.

There are several developments that will increase the sensitivity and flexibility of $870 \mu\text{m}$ VLBI in the near future. Next-generation VLBI backends (Doeleman et al. 2023) will allow an increase in data capture rates from 64 to 128 Gb/s (per observing frequency band), lowering detection thresholds by $\sqrt{2}$. Additional use of the Frequency Phase Transfer technique (FPT; Rioja et al. 2023) through simultaneous observations at 86, 230 and 345GHz will extend coherent integration times at higher frequencies, further increasing sensitivity. In optimal cases this increase will be the square root of the ratio of coherence times at 86GHz and 345GHz ($\sqrt{\tau_c(86)/\tau_c(345)}$). And the participation of more telescopes at high altitude sites will make the EHT array more robust against adverse weather conditions, increasing the opportunities for staging $870 \mu\text{m}$ VLBI observations (Raymond et al. 2021; Doeleman et al. 2023). Anticipated upgrades to the ALMA array will be exceptionally useful to advance $870 \mu\text{m}$ VLBI, and are planned on a similar timeline (~ 2030) as the ngEHT upgrade (Carpenter et al. 2023). In particular, the projected doubling of continuum bandwidth of ALMA will match the ngEHT specifications, and a sub-array capability at ALMA will enable simultaneous multi-band observations that benefit from FPT as noted above. In sum, the prospects for routine $870 \mu\text{m}$ VLBI in the near future are excellent.

⁵ General Relativistic Magnetohydrodynamic

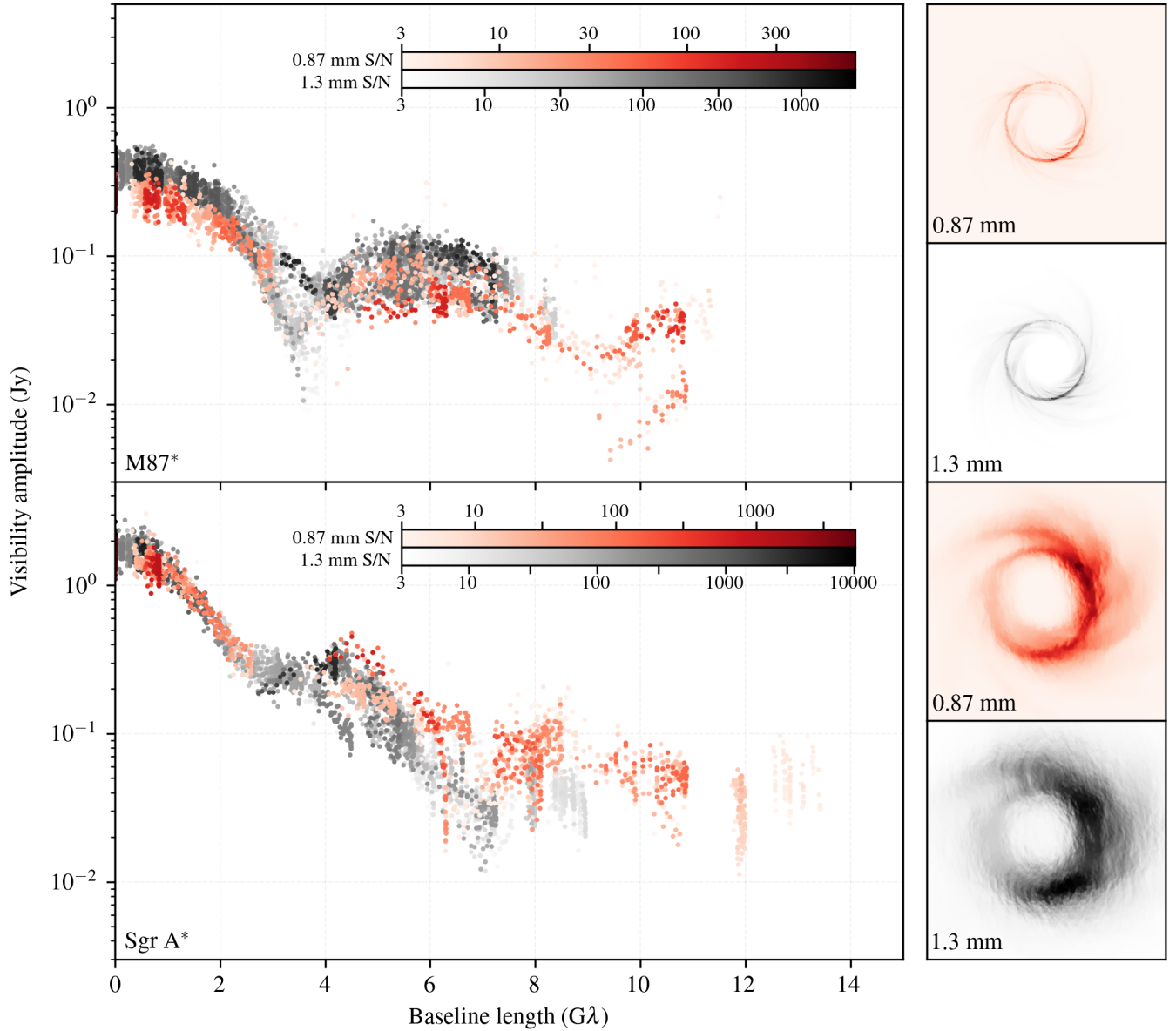


Figure 9. *Left:* Visibility amplitudes for simulated observations of M87* (top) and Sgr A* (bottom) at observing wavelengths of 1.3 mm (gray) and 0.87 mm (red). The synthetic data have been generated using the `ngensim` package assuming array specifications appropriate for the Phase 2 next-generation EHT array from Doeleman et al. (2023), including simultaneous dual-band observations, the use of the frequency phase transfer calibration technique, and 16 GHz of bandwidth at both frequencies. Data points are colored by their S/N on an integration time of 5 minutes, and data points with $S/N < 3$ have been flagged. *Right:* Images produced from GRMHD simulations of the M87* (top two panels; Event Horizon Telescope Collaboration et al. 2019e) and Sgr A* (bottom two panels; Event Horizon Telescope Collaboration et al. 2022b) accretion flows, used to generate the synthetic data shown in the left panels. Both simulations have been ray-traced at observing wavelengths of 1.3 mm (gray) and 0.87 mm (red), and the frequency-dependent effects of interstellar scattering have been applied to the Sgr A* images (Johnson 2016; Johnson et al. 2018).

5. CONCLUSIONS

VLBI fringe detections on baselines between ALMA-APEX, ALMA-IRAM30m, and ALMA-SMA have been achieved at $870 \mu\text{m}$ for multiple AGN sources. Signal-to-noise ratios were between approximately 10 and 70. Despite marginal weather conditions across the array, detections to multiple stations and sources were obtained. This work demonstrates that the EHT instrumentation is viable at $870 \mu\text{m}$ (345 GHz) and will provide a critical advance in array capability. EHT-wide observations at $870 \mu\text{m}$ would yield a fringe spacing of about $15 \mu\text{as}$, and with a full-track of coverage, would significantly enhance the fine details of the EHT images of AGN and horizon-scale targets (Doeleman et al. 2019, 2023; Johnson et al. 2023).

ACKNOWLEDGMENTS

This work was supported by the National Science Foundation (grants AST-1935980, AST-1743747, AST-1440254), an ALMA Cycle 5 North America Development Award, the Gordon and Betty Moore Foundation (awards GBMF3561, GBMF5278, and GBMF10423), and a generous gift from the Deepak Raghavan Family Foundation. Work on this project was conducted in part at the Black Hole Initiative at Harvard University (funded through grants 60477, 61479 and 62286 from the John Templeton Foundation; and grant GBMF8273 from the Gordon and Betty Moore Foundation). This work is partly based on observations carried out with the IRAM 30-m telescope and the NOEMA Interferometer. IRAM is supported by INSU/CNRS (France), MPG (Germany) and IGN (Spain). The IRAM NOEMA phasing project was supported by the European Research Council (ERC) Synergy Grant "BlackHoleCam: Imaging the Event Horizon of Black Holes" (grant 610058). The Submillimeter Array is a joint project between the Smithsonian Astrophysical Observatory and the Academia Sinica Institute of Astronomy and Astrophysics and is funded by the Smithsonian Institution and the Academia Sinica. The SMA gratefully acknowledges the efforts of its staff for supporting these observations, including those of the operator on duty, R. Howie. This publication is based on data acquired with the Atacama Pathfinder Experiment (APEX). APEX is a collaboration between the Max-Planck-Institut für Radioastronomie, the European Southern Observatory, and the Onsala Space Observatory. This work was an activity external to JPL, and effort by A.R. was not in their capacity as an employee of the Jet Propulsion Laboratory, California Institute of Technology. The Greenland Telescope (GLT) is supported by the the Ministry of Science and Technology (MOST) of Taiwan (103-2119-M-001-010-MY2, 105-2119-M-001-042, 106-2119-M-001-013, 107-2119-M-001-041, 108-2112-M-001-048, 109-2124-M-001-005, 110-2124-M-001-007) and the National Science and Technology Council (NSTC) of Taiwan (111-2124-M-001-005, 112-2124-M-001-014).

The Event Horizon Telescope Collaboration additionally thanks the following organizations and programs: the

Academia Sinica; the Academy of Finland (projects 274477, 284495, 312496, 315721); the Agencia Nacional de Investigación y Desarrollo (ANID), Chile via NCN19_058 (TITANs), Fondecyt 1221421 and BASAL FB210003; the Alexander von Humboldt Stiftung; an Alfred P. Sloan Research Fellowship; Allegro, the European ALMA Regional Centre node in the Netherlands, the NL astronomy research network NOVA and the astronomy institutes of the University of Amsterdam, Leiden University, and Radboud University; the ALMA North America Development Fund; the Astrophysics and High Energy Physics programme by MCIN (with funding from European Union NextGenerationEU, PRTR-C17I1); the Brinson Foundation; "la Caixa" Foundation (ID 100010434) through fellowship codes LCF/BQ/DI22/11940027 and LCF/BQ/DI22/11940030; Chandra DD7-18089X and TM6-17006X; the China Scholarship Council; the China Postdoctoral Science Foundation fellowships (2020M671266, 2022M712084); Consejo Nacional de Humanidades, Ciencia y Tecnología (CONAHCYT, Mexico, projects U0004-246083, U0004-259839, F0003-272050, M0037-279006, F0003-281692, 104497, 275201, 263356); the Colfuturo Scholarship; the Consejería de Economía, Conocimiento, Empresas y Universidad de la Junta de Andalucía (grant P18-FR-1769), the Consejo Superior de Investigaciones Científicas (grant 2019AEP112); the Delaney Family via the Delaney Family John A. Wheeler Chair at Perimeter Institute; Dirección General de Asuntos del Personal Académico-Universidad Nacional Autónoma de México (DGAPA-UNAM, projects IN112820 and IN108324); the Dutch Research Council (NWO) for the VICI award (grant 639.043.513), the grant OCENW.KLEIN.113, and the Dutch Black Hole Consortium (with project No. NWA 1292.19.202) of the research programme the National Science Agenda; the Dutch National Supercomputers, Cartesius and Snellius (NWO grant 2021.013); the EACOA Fellowship awarded by the East Asia Core Observatories Association, which consists of the Academia Sinica Institute of Astronomy and Astrophysics, the National Astronomical Observatory of Japan, Center for Astronomical Mega-Science, Chinese Academy of Sciences, and the Korea Astronomy and Space Science Institute; the European Union Horizon 2020 research and innovation programme under grant agreements RadioNet (No. 730562), M2FINDERS (No. 101018682) and FunFiCO (No. 777740); the European Research Council for advanced grant 'JETSET: Launching, propagation and emission of relativistic jets from binary mergers and across mass scales' (grant No. 884631); the European Horizon Europe staff exchange (SE) programme HORIZON-MSCA-2021-SE-01 grant NewFunFiCO (No. 10108625); the Horizon ERC Grants 2021 programme under grant agreement No. 101040021; the FAPESP (Fundação de Amparo à Pesquisa do Estado de São Paulo) under grant 2021/01183-8; the Fondo CAS-ANID folio CAS220010; the Generalitat Valenciana (grants APOSTD/2018/177 and ASFAE/2022/018) and GenT Program (project CIDEAGENT/2018/021); the Institute for Advanced Study; the Istituto Nazionale di

Fisica Nucleare (INFN) sezione di Napoli, iniziative specifiche TEONGRAV; the International Max Planck Research School for Astronomy and Astrophysics at the Universities of Bonn and Cologne; DFG research grant “Jet physics on horizon scales and beyond” (grant No. 443220636); Joint Columbia/Flatiron Postdoctoral Fellowship (research at the Flatiron Institute is supported by the Simons Foundation); the Japan Ministry of Education, Culture, Sports, Science and Technology (MEXT; grant JPMXP1020200109); the Japan Society for the Promotion of Science (JSPS) Grant-in-Aid for JSPS Research Fellowship (JP17J08829); the Joint Institute for Computational Fundamental Science, Japan; the Key Research Program of Frontier Sciences, Chinese Academy of Sciences (CAS, grants QYZDJ-SSW-SLH057, QYZDJSSW-SYS008, ZDBS-LY-SLH011); the Leverhulme Trust Early Career Research Fellowship; the Max-Planck-Gesellschaft (MPG); the Max Planck Partner Group of the MPG and the CAS; the MEXT/JSPS KAKENHI (grants 18KK0090, JP21H01137, JP18H03721, JP18K13594, 18K03709, JP19K14761, 18H01245, 25120007, 19H01943, 21H01137, 21H04488, 22H00157, 23K03453); the MICINN Research Projects PID2019-108995GB-C22, PID2022-140888NB-C22; the MIT International Science and Technology Initiatives (MISTI) Funds; the Ministry of Science and Technology (MOST) of Taiwan (105-2112-M-001-025-MY3, 106-2112-M-001-011, 106-2119-M-001-027, 106-2923-M-001-005, 107-2119-M-001-017, 107-2119-M-001-020, 107-2119-M-110-005, 107-2923-M-001-009, 108-2112-M-001-051, 108-2923-M-001-002, 109-2112-M-001-025, 109-2923-M-001-001, 110-2112-M-001-033, 110-2923-M-001-001, and 112-2112-M-003-010-MY3); the Ministry of Education (MoE) of Taiwan Yushan Young Scholar Program; the Physics Division, National Center for Theoretical Sciences of Taiwan; the National Aeronautics and Space Administration (NASA, Fermi Guest Investigator grant 80NSSC23K1508, NASA Astrophysics Theory Program grant 80NSSC20K0527, NASA NuSTAR award 80NSSC20K0645); NASA Hubble Fellowship grants HST-HF2-51431.001-A, HST-HF2-51482.001-A awarded by the Space Telescope Science Institute, which is operated by the Association of Universities for Research in Astronomy, Inc., for NASA, under contract NAS5-26555; the National Institute of Natural Sciences (NINS) of Japan; the National Key Research and Development Program of China (grant 2016YFA0400704, 2017YFA0402703, 2016YFA0400702); the National Science and Technology Council (NSTC, grants NSTC 111-2112-M-001 -041, NSTC 111-2124-M-001-005, NSTC 112-2124-M-001-014); the US National Science Foundation (NSF, grants AST-0096454, AST-0352953, AST-0521233, AST-0705062, AST-0905844, AST-0922984, AST-1126433, OIA-1126433, AST-1140030, DGE-1144085, AST-1207704, AST-1207730, AST-1207752, MRI-1228509, OPP-1248097, AST-1310896, AST-1555365, AST-1614868, AST-1615796, AST-1715061, AST-1716327, AST-1726637, OISE-1743747, AST-1816420, AST-1952099, AST-2034306, AST-2205908, AST-2307887); NSF Astronomy and Astrophysics Post-

doctoral Fellowship (AST-1903847); the Natural Science Foundation of China (grants 11650110427, 10625314, 11721303, 11725312, 11873028, 11933007, 11991052, 11991053, 12192220, 12192223, 12273022, 12325302, 12303021); the Natural Sciences and Engineering Research Council of Canada (NSERC, including a Discovery Grant and the NSERC Alexander Graham Bell Canada Graduate Scholarships-Doctoral Program); the National Research Foundation of Korea (the Global PhD Fellowship Grant: grants NRF-2015H1A2A1033752, the Korea Research Fellowship Program: NRF-2015H1D3A1066561, Brain Pool Program: 2019H1D3A1A01102564, Basic Research Support Grant 2019R1F1A1059721, 2021R1A6A3A01086420, 2022R1C1C1005255, 2022R1F1A1075115); Netherlands Research School for Astronomy (NOVA) Virtual Institute of Accretion (VIA) postdoctoral fellowships; NOIR-Lab, which is managed by the Association of Universities for Research in Astronomy (AURA) under a cooperative agreement with the National Science Foundation; Onsala Space Observatory (OSO) national infrastructure, for the provisioning of its facilities/observational support (OSO receives funding through the Swedish Research Council under grant 2017-00648); the Perimeter Institute for Theoretical Physics (research at Perimeter Institute is supported by the Government of Canada through the Department of Innovation, Science and Economic Development and by the Province of Ontario through the Ministry of Research, Innovation and Science); the Portuguese Foundation for Science and Technology (FCT) grants (Individual CEEC program - 5th edition, <https://doi.org/10.54499/UIDB/04106/2020>, <https://doi.org/10.54499/UIDP/04106/2020>, PTDC/FIS-AST/3041/2020, CERN/FIS-PAR/0024/2021, 2022.04560.PTDC); the Princeton Gravity Initiative; the Spanish Ministerio de Ciencia e Innovación (grants PGC2018-098915-B-C21, AYA2016-80889-P, PID2019-108995GB-C21, PID2020-117404GB-C21); the University of Pretoria for financial aid in the provision of the new Cluster Server nodes and SuperMicro (USA) for a SEEDING GRANT approved toward these nodes in 2020; the Shanghai Municipality orientation program of basic research for international scientists (grant no. 22JC1410600); the Shanghai Pilot Program for Basic Research, Chinese Academy of Science, Shanghai Branch (JCYJ-SHFY-2021-013); the State Agency for Research of the Spanish MCIU through the “Center of Excellence Severo Ochoa” award for the Instituto de Astrofísica de Andalucía (SEV-2017- 0709); the Spanish Ministry for Science and Innovation grant CEX2021-001131-S funded by MCIN/AEI/10.13039/501100011033; the Spinoza Prize SPI 78-409; the South African Research Chairs Initiative, through the South African Radio Astronomy Observatory (SARAO, grant ID 77948), which is a facility of the National Research Foundation (NRF), an agency of the Department of Science and Innovation (DSI) of South Africa; the Swedish Research Council (VR); the Taplin Fellowship; the Toray Science Foundation; the UK Science and Technology Facilities Council (grant no. ST/X508329/1); the US Department of Energy (USDOE) through the Los

Alamos National Laboratory (operated by Triad National Security, LLC, for the National Nuclear Security Administration of the USDOE, contract 89233218CNA000001); and the YCAA Prize Postdoctoral Fellowship.

We thank the staff at the participating observatories, correlation centers, and institutions for their enthusiastic support. This work made use of the following ALMA data: ADS/JAO.ALMA#2011.0.00010.E for the VLBI sessions and ADS/JAO.ALMA#2011.0.00012.E for the Band 7 test data as well as ADS/JAO.ALMA#2016.1.01154.V. ALMA is a partnership of ESO (representing its member states), NSF (USA) and NINS (Japan), together with NRC (Canada), NSTC and ASIAA (Taiwan), and KASI (Republic of Korea), in cooperation with the Republic of Chile. The Joint ALMA Observatory is operated by ESO, AUI/NRAO and NAOJ. See <https://almascience.eso.org/almadata/ec/eht-2018> for more detail and access to the data. The NRAO is a facility of the NSF operated under cooperative agreement by AUI. This research used resources of the Oak Ridge Leadership Computing Facility at the Oak Ridge National Laboratory, which is supported by the Office of Science of the U.S. Department of Energy under contract No. DE-AC05-

00OR22725; the ASTROVIVES FEDER infrastructure, with project code IDIFEDER-2021-086; the computing cluster of Shanghai VLBI correlator supported by the Special Fund for Astronomy from the Ministry of Finance in China; We also thank the Center for Computational Astrophysics, National Astronomical Observatory of Japan. This work was supported by FAPESP (Fundacao de Amparo a Pesquisa do Estado de Sao Paulo) under grant 2021/01183-8.

The EHTC has received generous donations of FPGA chips from Xilinx Inc., under the Xilinx University Program. The EHTC has benefited from technology shared under open-source license by the Collaboration for Astronomy Signal Processing and Electronics Research (CASPER). The EHT project is grateful to T4Science and Microsemi for their assistance with hydrogen masers. This research has made use of NASA's Astrophysics Data System. We gratefully acknowledge the support provided by the extended staff of the ALMA, from the inception of the ALMA Phasing Project through the observational campaigns of 2017 and 2018. We would like to thank A. Deller and W. Brisken for EHT-specific support with the use of DiFX. We acknowledge the significance that Maunakea, where the SMA EHT station is located, has for the indigenous Hawaiian people.

REFERENCES

- Baath, L. B., Padin, S., Woody, D., et al. 1991, *A&A*, 241, L1
- Baath, L. B., Rogers, A. E. E., Inoue, M., et al. 1992, *A&A*, 257, 31
- Belitsky, V., Lapkin, I., Fredrixon, M., et al. 2018, *A&A*, 612, A23, doi: [10.1051/0004-6361/201731458](https://doi.org/10.1051/0004-6361/201731458)
- Blackburn, L., Chan, C.-k., Crew, G. B., et al. 2019, *ApJ*, 882, 23, doi: [10.3847/1538-4357/ab328d](https://doi.org/10.3847/1538-4357/ab328d)
- Carpenter, J., Brogan, C., Iono, D., & Mroczkowski, T. 2023, in *Physics and Chemistry of Star Formation: The Dynamical ISM Across Time and Spatial Scales*, 304
- Carter, M., Lazareff, B., Maier, D., et al. 2012, *A&A*, 538, A89, doi: [10.1051/0004-6361/201118452](https://doi.org/10.1051/0004-6361/201118452)
- Chael, A., Issaoun, S., Pesce, D. W., et al. 2023, *ApJ*, 945, 40, doi: [10.3847/1538-4357/acb7e4](https://doi.org/10.3847/1538-4357/acb7e4)
- Chen, M.-T., Asada, K., Matsushita, S., et al. 2023, *PASP*, 135, 095001, doi: [10.1088/1538-3873/acf072](https://doi.org/10.1088/1538-3873/acf072)
- Chenu, J. Y., Carter, M., Maier, D., et al. 2007, in *2007 Joint 32nd International Conference on Infrared and Millimeter Waves and the 15th International Conference on Terahertz Electronics*, 176–177
- Chenu, J.-Y., Navarrini, A., Bortolotti, Y., et al. 2016, *IEEE Transactions on Terahertz Science and Technology*, 6, 223, doi: [10.1109/TTHZ.2016.2525762](https://doi.org/10.1109/TTHZ.2016.2525762)
- Crew, G. B., Goddi, C., Matthews, L. D., et al. 2023, *Publications of the Astronomical Society of the Pacific*, 135, 025002, doi: [10.1088/1538-3873/acb348](https://doi.org/10.1088/1538-3873/acb348)
- Deller, A. T., Brisken, W. F., Phillips, C. J., et al. 2011, *PASP*, 123, 275, doi: [10.1086/658907](https://doi.org/10.1086/658907)
- Doeleman, S., Mai, T., Rogers, A. E. E., et al. 2011, *PASP*, 123, 582, doi: [10.1086/660156](https://doi.org/10.1086/660156)
- Doeleman, S., Blackburn, L., Dexter, J., et al. 2019, in *Bulletin of the American Astronomical Society*, Vol. 51, 256
- Doeleman, S. S., Phillips, R. B., Rogers, A. E. E., et al. 2002, in *Proceedings of the 6th EVN Symposium*, 223
- Doeleman, S. S., Weintraub, J., Rogers, A. E. E., et al. 2008, *Nature*, 455, 78, doi: [10.1038/nature07245](https://doi.org/10.1038/nature07245)
- Doeleman, S. S., Fish, V. L., Schenck, D. E., et al. 2012, *Science*, 338, 355, doi: [10.1126/science.1224768](https://doi.org/10.1126/science.1224768)
- Doeleman, S. S., Barrett, J., Blackburn, L., et al. 2023, *Galaxies*, 11, 107, doi: [10.3390/galaxies11050107](https://doi.org/10.3390/galaxies11050107)
- Event Horizon Telescope Collaboration, Akiyama, K., Alberdi, A., et al. 2019a, *ApJL*, 875, L1, doi: [10.3847/2041-8213/ab0ec7](https://doi.org/10.3847/2041-8213/ab0ec7)
- , 2019b, *ApJL*, 875, L2, doi: [10.3847/2041-8213/ab0c96](https://doi.org/10.3847/2041-8213/ab0c96)
- , 2019c, *ApJL*, 875, L4, doi: [10.3847/2041-8213/ab0e85](https://doi.org/10.3847/2041-8213/ab0e85)
- , 2019d, *ApJL*, 875, L3, doi: [10.3847/2041-8213/ab0c57](https://doi.org/10.3847/2041-8213/ab0c57)
- , 2019e, *ApJL*, 875, L5, doi: [10.3847/2041-8213/ab0f43](https://doi.org/10.3847/2041-8213/ab0f43)
- Event Horizon Telescope Collaboration, Akiyama, K., Algaba, J. C., et al. 2021, *The Astrophysical Journal Letters*, 910, L13, doi: [10.3847/2041-8213/abe4de](https://doi.org/10.3847/2041-8213/abe4de)
- Event Horizon Telescope Collaboration, Akiyama, K., Alberdi, A., et al. 2022a, *ApJL*, 930, L12, doi: [10.3847/2041-8213/ac6674](https://doi.org/10.3847/2041-8213/ac6674)
- , 2022b, *ApJL*, 930, L16, doi: [10.3847/2041-8213/ac6672](https://doi.org/10.3847/2041-8213/ac6672)
- , 2024, *A&A*, 681, A79, doi: [10.1051/0004-6361/202347932](https://doi.org/10.1051/0004-6361/202347932)

- Goddi, C., Martí-Vidal, I., Messias, H., et al. 2019, *PASP*, 131, 075003, doi: [10.1088/1538-3873/ab136a](https://doi.org/10.1088/1538-3873/ab136a)
- Greve, A., & Bremer, M. 2010, *Thermal Design and Thermal Behaviour of Radio Telescopes and their Enclosures*, Vol. 364, doi: [10.1007/978-3-642-03866-2](https://doi.org/10.1007/978-3-642-03866-2)
- Greve, A., Torres, M., Wink, J. E., et al. 1995, *A&A*, 299, L33
- Greve, A., Könönen, P., Graham, D. A., et al. 2002, *A&A*, 390, L19, doi: [10.1051/0004-6361:20020893](https://doi.org/10.1051/0004-6361:20020893)
- Hada, K., Doi, A., Kino, M., et al. 2011, *Nature*, 477, 185, doi: [10.1038/nature10387](https://doi.org/10.1038/nature10387)
- Han, C.-C., Chen, M.-T., Huang, Y.-D., et al. 2018, in *Society of Photo-Optical Instrumentation Engineers (SPIE) Conference Series*, Vol. 10708, Millimeter, Submillimeter, and Far-Infrared Detectors and Instrumentation for Astronomy IX, ed. J. Zmuidzinas & J.-R. Gao, 1070835
- Inoue, M., Algaba-Marcos, J. C., Asada, K., et al. 2014, *Radio Science*, 49, 564, doi: [10.1002/2014RS005450](https://doi.org/10.1002/2014RS005450)
- Issaoun, S., Johnson, M. D., Blackburn, L., et al. 2019, *ApJ*, 871, 30, doi: [10.3847/1538-4357/aaf732](https://doi.org/10.3847/1538-4357/aaf732)
- Issaoun, S., Wielgus, M., Jorstad, S., et al. 2022, *ApJ*, 934, 145, doi: [10.3847/1538-4357/ac7a40](https://doi.org/10.3847/1538-4357/ac7a40)
- Janssen, M., Falcke, H., Kadler, M., et al. 2021, *Nature Astronomy*, 5, 1017, doi: [10.1038/s41550-021-01417-w](https://doi.org/10.1038/s41550-021-01417-w)
- Janssen, M., Goddi, C., van Bemmell, I. M., et al. 2019, *A&A*, 626, A75, doi: [10.1051/0004-6361/201935181](https://doi.org/10.1051/0004-6361/201935181)
- Johnson, M. D. 2016, *ApJ*, 833, 74, doi: [10.3847/1538-4357/833/1/74](https://doi.org/10.3847/1538-4357/833/1/74)
- Johnson, M. D., Narayan, R., Psaltis, D., et al. 2018, *ApJ*, 865, 104, doi: [10.3847/1538-4357/aadceff](https://doi.org/10.3847/1538-4357/aadceff)
- Johnson, M. D., Lupsasca, A., Strominger, A., et al. 2020, *Science Advances*, 6, eaaz1310, doi: [10.1126/sciadv.aaz1310](https://doi.org/10.1126/sciadv.aaz1310)
- Johnson, M. D., Akiyama, K., Blackburn, L., et al. 2023, *Galaxies*, 11, 61, doi: [10.3390/galaxies11030061](https://doi.org/10.3390/galaxies11030061)
- Jorstad, S., Wielgus, M., Lico, R., et al. 2023, *ApJ*, 943, 170, doi: [10.3847/1538-4357/aca8a8](https://doi.org/10.3847/1538-4357/aca8a8)
- Kerr, A. R., Pan, S.-K., Claude, S. M. X., et al. 2014, *IEEE Transactions on Terahertz Science and Technology*, 4, 201, doi: [10.1109/TTHZ.2014.2302537](https://doi.org/10.1109/TTHZ.2014.2302537)
- Kim, J.-y., Krichbaum, T. P., Broderick, A. E., et al. 2020, *Astronomy & Astrophysics*, 640, A69, doi: [10.1051/0004-6361/202037493](https://doi.org/10.1051/0004-6361/202037493)
- Klein, T., Ciechanowicz, M., Leinz, C., et al. 2014, *IEEE Transactions on Terahertz Science and Technology*, 4, 588, doi: [10.1109/TTHZ.2014.2342498](https://doi.org/10.1109/TTHZ.2014.2342498)
- Klein, T., Ciechanowicz, M., Leinz, C., et al. 2014, *IEEE Transactions on Terahertz Science and Technology*, 4, 588, doi: [10.1109/TTHZ.2014.2342498](https://doi.org/10.1109/TTHZ.2014.2342498)
- Koay, J. Y., Matsushita, S., Asada, K., et al. 2020, in *Ground-based and Airborne Telescopes VIII*, ed. H. K. Marshall, J. Spyromilio, & T. Usuda, Vol. 11445, *International Society for Optics and Photonics (SPIE)*, 114450Q. <https://doi.org/10.1117/12.2561491>
- Krichbaum, T. P., Graham, D. A., Greve, A., et al. 1997, *A&A*, 323, L17
- Krichbaum, T. P., Graham, D. A., Witzel, A., et al. 1998, *A&A*, 335, L106
- Krichbaum, T. P., Graham, D. A., Alef, W., et al. 2002, in *Proceedings of the 6th EVN Symposium*, 125
- Levy, R., Antennas, I., & Society, P. 1996, *Structural Engineering of Microwave Antennas: For Electrical, Mechanical, and Civil Engineering (IEEE Press)*. https://books.google.com/books?id=qPV_QgAACAAJ
- Liebe, H. J. 1985, *Radio Science*, 20, 1069, doi: [10.1029/RS020i005p01069](https://doi.org/10.1029/RS020i005p01069)
- Lo, W.-P., Asada, K., Matsushita, S., et al. 2023, *The Astrophysical Journal*, 950, 10, doi: [10.3847/1538-4357/acc855](https://doi.org/10.3847/1538-4357/acc855)
- Lobanov, A. P. 1998, *A&A*, 330, 79, doi: [10.48550/arXiv.astro-ph/9712132](https://doi.org/10.48550/arXiv.astro-ph/9712132)
- Mahieu, S., Maier, D., Lazareff, B., et al. 2012, *IEEE Transactions on Terahertz Science and Technology*, 2, 29, doi: [10.1109/TTHZ.2011.2177734](https://doi.org/10.1109/TTHZ.2011.2177734)
- Maier, D., Barbier, A., Lazareff, B., & Schuster, K. F. 2005, in *Sixteenth International Symposium on Space Terahertz Technology*, 428–431
- Maier, D., Reverdy, J., Billon-Pierron, D., & Barbier, A. 2012, *IEEE Transactions on Terahertz Science and Technology*, 2, 215, doi: [10.1109/TTHZ.2011.2180609](https://doi.org/10.1109/TTHZ.2011.2180609)
- Mangum, J. G., Baars, J. W. M., Greve, A., et al. 2006, *PASP*, 118, 1257, doi: [10.1086/508298](https://doi.org/10.1086/508298)
- Martí-Vidal, I., Roy, A., Conway, J., & Zensus, A. J. 2016, *A&A*, 587, A143, doi: [10.1051/0004-6361/201526063](https://doi.org/10.1051/0004-6361/201526063)
- Matsushita, S., Matsuo, H., Pardo, J. R., & Radford, S. J. E. 1999, *PASJ*, 51, 603, doi: [10.1093/pasj/51.5.603](https://doi.org/10.1093/pasj/51.5.603)
- Matsushita, S., Asada, K., Martin-Cocher, P. L., et al. 2016, *Publications of the Astronomical Society of the Pacific*, 129, 025001, doi: [10.1088/1538-3873/129/972/025001](https://doi.org/10.1088/1538-3873/129/972/025001)
- Matsushita, S., Asada, K., Inoue, M., et al. 2018, in *Society of Photo-Optical Instrumentation Engineers (SPIE) Conference Series*, Vol. 10700, *Ground-based and Airborne Telescopes VII*, ed. H. K. Marshall & J. Spyromilio, 1070029
- Matsushita, S., Martin-Cocher, P. L., Paine, S. N., et al. 2022, *PASP*, 134, 125002, doi: [10.1088/1538-3873/acac51](https://doi.org/10.1088/1538-3873/acac51)
- Matthews, L. D., Crew, G. B., Doeleman, S. S., et al. 2018, *PASP*, 130, 015002, doi: [10.1088/1538-3873/aa9c3d](https://doi.org/10.1088/1538-3873/aa9c3d)
- Meledin, D., Lapkin, I., Fredrixon, M., et al. 2022, *A&A*, 668, A2, doi: [10.1051/0004-6361/202244211](https://doi.org/10.1051/0004-6361/202244211)

- Okino, H., Akiyama, K., Asada, K., et al. 2022, *The Astrophysical Journal*, 940, 65, doi: [10.3847/1538-4357/ac97e5](https://doi.org/10.3847/1538-4357/ac97e5)
- Padin, S., Woody, D. P., Hodges, M. W., et al. 1990, *ApJL*, 360, L11, doi: [10.1086/185800](https://doi.org/10.1086/185800)
- Paine, S. 2022, doi: [10.5281/zenodo.6774378](https://doi.org/10.5281/zenodo.6774378)
- Palumbo, D. C. M., Wong, G. N., Chael, A., & Johnson, M. D. 2023, *ApJL*, 952, L31, doi: [10.3847/2041-8213/ace630](https://doi.org/10.3847/2041-8213/ace630)
- Paraschos, G. F., Kim, J. Y., Wielgus, M., et al. 2024, *A&A*, 682, L3, doi: [10.1051/0004-6361/202348308](https://doi.org/10.1051/0004-6361/202348308)
- Pesce, D. W., Palumbo, D. C. M., Narayan, R., et al. 2021, *ApJ*, 923, 260, doi: [10.3847/1538-4357/ac2eb5](https://doi.org/10.3847/1538-4357/ac2eb5)
- Primiani, R. A., Young, K. H., Young, A., et al. 2016, *Journal of Astronomical Instrumentation*, 5, 1641006, doi: [10.1142/S2251171716410063](https://doi.org/10.1142/S2251171716410063)
- Raffin, P., Ho, P. T. P., Asada, K., et al. 2016, in *Society of Photo-Optical Instrumentation Engineers (SPIE) Conference Series*, Vol. 9906, *Ground-based and Airborne Telescopes VI*, ed. H. J. Hall, R. Gilmozzi, & H. K. Marshall, 99060U
- Ramakrishnan, V., Nagar, N., Arratia, V., et al. 2023, *Galaxies*, 11, 15, doi: [10.3390/galaxies11010015](https://doi.org/10.3390/galaxies11010015)
- Raymond, A. W., Palumbo, D., Paine, S. N., et al. 2021, *The Astrophysical Journal Supplement Series*, 253, 5, doi: [10.3847/1538-3881/abc3c3](https://doi.org/10.3847/1538-3881/abc3c3)
- Readhead, A. C. S., Mason, C. R., Mofett, A. T., et al. 1983, *Nature*, 303, 504, doi: [10.1038/303504a0](https://doi.org/10.1038/303504a0)
- Rioja, M. J., Dodson, R., & Asaki, Y. 2023, *Galaxies*, 11, 16, doi: [10.3390/galaxies11010016](https://doi.org/10.3390/galaxies11010016)
- Rogers, A. E., & Moran, J. M. 1981, *IEEE Transactions on Instrumentation and Measurement*, IM-30, 283, doi: [10.1109/TIM.1981.6312409](https://doi.org/10.1109/TIM.1981.6312409)
- Rogers, A. E. E., Doeleman, S. S., & Moran, J. M. 1995, *AJ*, 109, 1391, doi: [10.1086/117371](https://doi.org/10.1086/117371)
- Rogers, A. E. E., Moffet, A. T., Backer, D. C., & Moran, J. M. 1984, *Radio Science*, 19, 1552, doi: [10.1029/RS019i006p01552](https://doi.org/10.1029/RS019i006p01552)
- Thompson, A. R., Moran, J. M., & Swenson, Jr., G. W. 2017, *Interferometry and Synthesis in Radio Astronomy*, 3rd Edition, doi: [10.1007/978-3-319-44431-4](https://doi.org/10.1007/978-3-319-44431-4)
- Tong, C. Y. E., Blundell, R., Megerian, K. G., et al. 2005, *IEEE Transactions on Applied Superconductivity*, 15, 490, doi: [10.1109/TASC.2005.849885](https://doi.org/10.1109/TASC.2005.849885)
- Tong, C.-Y. E., Grimes, P., Blundell, R., Wang, M.-J., & Noguchi, T. 2013, *IEEE Transactions on Terahertz Science and Technology*, 3, 428, doi: [10.1109/TTHZ.2013.2259624](https://doi.org/10.1109/TTHZ.2013.2259624)
- Treuhaft, R. N., & Lanyi, G. E. 1987, *Radio Science*, 22, 251, doi: <https://doi.org/10.1029/RS022i002p00251>
- Tuccari, G., Alef, W., Wunderlich, M., et al. 2017, in 23rd *European VLBI Group for Geodesy and Astrometry Working Meeting*, ed. R. Haas & G. Elgered, 78–80
- Vertatschitsch, L., Primiani, R., Young, A., et al. 2015, *PASP*, 127, 1226, doi: [10.1086/684513](https://doi.org/10.1086/684513)
- Whitney, A. R., Cappallo, R., Aldrich, W., et al. 2004, *Radio Science*, 39, doi: [10.1029/2002RS002820](https://doi.org/10.1029/2002RS002820)
- Wielgus, M., Issaoun, S., Martí-Vidal, I., et al. 2024, *A&A*, 682, A97, doi: [10.1051/0004-6361/202347772](https://doi.org/10.1051/0004-6361/202347772)
- Young, A., Primiani, R., Weintroub, J., et al. 2016, in 2016 *IEEE International Symposium on Phased Array Systems and Technology (PAST)*, 1–8
- Zhao, G.-Y., Gómez, J. L., Fuentes, A., et al. 2022, *The Astrophysical Journal*, 932, 72, doi: [10.3847/1538-4357/ac6b9c](https://doi.org/10.3847/1538-4357/ac6b9c)